Deep-Cycle Turbulence in the Upper Pacific Equatorial Ocean: Characterization by LES and Heat Flux Parameterization

HIEU T. PHAM,[a] SUTANU SARKAR,[a,b] WILLIAM D. SMYTH,[c] JAMES N. MOUM,[c] AND SALLY J. WARNER[d]

[a] *Mechanical and Aerospace Engineering, University of California, San Diego, La Jolla, California*
[b] *Scripps Institution of Oceanography, University of California, San Diego, La Jolla, California*
[c] *College of Earth, Ocean and Atmospheric Science, Oregon State University, Corvallis, Oregon*
[d] *Department of Physics and Environmental Studies, Brandeis University, Waltham, Massachusetts*

(Manuscript received 30 January 2023, in final form 23 November 2023, accepted 29 November 2023)

ABSTRACT: Observations in the Pacific Equatorial Undercurrents (EUC) show that the nighttime deep-cycle turbulence (DCT) in the marginal-instability (MI) layer of the EUC exhibits seasonal variability that can modulate heat transport and sea surface temperature. Large-eddy simulations (LES), spanning a wide range of control parameters, are performed to identify the key processes that influence the turbulent heat flux at multiple time scales ranging from turbulent (minutes to hours) to daily to seasonal. The control parameters include wind stress, convective surface heat flux, shear magnitude, and thickness of the MI layer. In the LES, DCT occurs in discrete bursts during the night, exhibits high temporal variability within a burst, and modulates the mixed layer depth. At the daily time scale, turbulent heat flux generally increases with increasing wind stress, MI-layer shear, or nighttime convection. Convection is found to be important to mixing under weak wind, weak shear conditions. A parameterization for the daily averaged turbulent heat flux is developed from the LES suite to infer the variability of heat flux at the seasonal time scale. The LES-based parameterized heat flux, which takes into account the effects of all control parameters, exhibits a seasonal variability that is similar to the observed heat flux from the χ-pods.

KEYWORDS: Ocean dynamics; Turbulence; Mixing; Large eddy simulations; Parameterization; Seasonal variability

1. Introduction

Sea surface temperature plays an important role in air–sea interaction, and coupled climate models require its accurate prediction. Observations in the Pacific equatorial ocean in recent decades reveal that temperature in the mixed layer (ML) is strongly affected by the subsurface turbulent heat flux associated with deep-cycle turbulence (DCT), which occurs at night on the upper flank of the Equatorial Undercurrent (EUC) (Moum and Caldwell 1985; Hebert et al. 1992; Lien et al. 1996; Moum et al. 2013; Warner and Moum 2019). Recent large-scale regional models (Pei et al. 2020; Cherian et al. 2021) also indicate the importance of the DCT subsurface heat flux in this region, as well as at the Atlantic equatorial ocean where the undercurrent has a diurnal cycle of shear and stratification (Wenegrat and McPhaden 2015) and DCT (Moum et al. 2022).

The DCT is supported by marginal instability (MI) since the gradient Richardson number (Ri_g) in the layer where it develops clusters around the critical value of 0.25 for shear instability (Smyth and Moum 2013; Smyth 2020). Previous studies suggested that the heat flux depends not only on flow conditions local to the MI layer but also on surface forcing (Lien et al. 1995; Skyllingstad et al. 1999; Smyth et al. 2021, hereafter S21). It also leads to seasonal warming of the ML during boreal spring and cooling during autumn (Moum et al. 2013; Pham et al. 2017).

S21 used moored observations to identify the most important parameters governing the deep cycle, focusing on the parameterization of the turbulent kinetic energy dissipation rate. Using large-eddy simulations (LES), Whitt et al. (2022, hereafter W22), introduced a parameterization for the turbulent buoyancy flux that used different control parameters from those in S21. In the present study, we extend the work of S21 and W22 to examine the seasonal cycle of turbulent heat flux. To do this, we employ LES to characterize DCT over multiple time scales in a parametric study that spans the range of conditions in observations.

On the daily time scale, previous observational and numerical studies suggest the depth-averaged dissipation rate (ε) of the DCT scales with the friction velocity (u_*) and some bulk measure of the shear (S^b) through the scaling: $\varepsilon = \gamma_\varepsilon u_*^2 S^b$, where the proportionality constant (γ_ε) and the quantification of S^b vary significantly among the studies. For example, using turbulence measurements during a 12-day cruise during the Tropic Heat I experiment (November–December 1984), Moum et al. (1989, hereafter M89) correlated the depth-averaged dissipation rate with the wind and the depth-averaged shear between 10- and 25-m depths and found $\gamma_\varepsilon \approx 0.19$. In contrast, S21 analyzed the multiyear record of turbulence measurements from moored χ-pods (Perlin and Moum 2012) and suggested that the depth-averaged dissipation rate is proportional to $(u_*^2 S^b)^2$, in which case dimensionality requires the inclusion of another dimensional parameter, chosen to be the short-wave buoyancy flux (B_{SW}). Furthermore, they specified S^b to be the averaged shear in the MI layer. Using LES embedded inside a regional

Denotes content that is immediately available upon publication as open access.

Corresponding author: Hieu T. Pham, h8pham@ucsd.edu

Publisher's Note: This article was revised on 1 February 2024 to correct two errors when originally published: the variable S_b, whose subscript mistakenly appeared as a superscript throughout the text, and removing the erroneous exponent 2 that appeared in the term $u_*^2 S_b$ in the seventh paragraph of section 5.

DOI: 10.1175/JPO-D-23-0015.1

MITgcm simulation with realistic surface forcing, W22 found that the peak turbulent buoyancy flux ($J_b^{\max}$) in the MI layer can be parameterized as $J_b^{\max} = -\gamma_{J_b}^{\max} u_*^2 S^b$, where the coefficient $\gamma_{J_b}^{\max} = 0.16$ and S^b is the bulk shear across both the surface mixed layer and the MI layer. The difference between the scalings of M89, S21, and W22 motivate us to reexamine how the DCT can be parameterized on a daily average basis given the important consequences for quantification of turbulent heat flux and thus the warming or cooling of sea surface temperature.

Parameterization studies have inherent limitations linked in part to the observational data employed. Shipboard profiling experiments yield detailed vertical resolution but short time series so that surface forcing and background flow condition are limited to a narrow range. The χ-pods yield long time series but relatively coarse vertical resolution which can affect the parameterization quality. The LES simulation in W22 produces high-resolution turbulence data but the forcing parameters are limited to the conditions during the period between October and November 1985. Expanding from the work of W22, we use high-resolution LES to simulate DCT over a wide range of forcing and, additionally, utilize the long-term turbulence measurements from the χ-pods to understand what causes the difference between the scalings in the previous studies and further explore other parameters that can influence the turbulence.

To evaluate the parameterization of DCT, it is necessary to characterize the DCT at turbulence time scales (i.e., minutes to hours). Previous small-scale studies (using shipboard microstructure data or LES) have shown the evolution of the DCT to be complex. It involves the evening descent of a near-surface shear layer which triggers local shear instabilities in the MI layer leading to DCT (Smyth et al. 2011, 2013; Pham et al. 2013). Often, DCT occurs in multiple bursts and exhibits high temporal and spatial fluctuation (M89; Smyth et al. 2017) and so does the heat flux (Sarkar and Pham 2019). Wang and Müller (2002) showed that DCT can be triggered by nighttime convection in the absence of wind stress. Nighttime convection affects the parameterization of turbulence in the surface mixed layer (Lombardo and Gregg 1989); however, its role in the DCT parameterization has not been evaluated. Here, we characterize DCT in a systematic parametric study using LES, specifically addressing the following questions regarding the response of DCT and the associated turbulent heat flux:

- How would the variation in the wind stress, surface buoyancy fluxes, and background conditions that are found in observations affect the intensity and vertical extent of the bursts of DCT?
- What importance does convection have in the DCT relative to other forcings such as wind and EUC shear?
- Can the heat flux be parameterized using the LES data? How does a linear combination of governing parameters compare with previous parameterization? Since the LES is designed to span a wide range of EUC conditions, how does the LES-based parameterization compare with the seasonal cycle in observations?

The paper is organized as follows. The parameter space and description of the LES model are provided in section 2.

TABLE 1. Definition of parameters used in discussion.

Parameters	Definition
$Q_{\rm sw}$, $B_{\rm sw}$	Solar heat flux and corresponding buoyancy flux
$Q_{\rm ns}$, B_0	Nonsolar surface heat flux and corresponding buoyancy flux
τ_w	Wind stress
u_*	Frictional velocity
$h_{\rm MI}$	Thickness of marginal instability (MI) layer
MLD	Mixed layer depth
$z^{\rm MI}$	Depth where Ri_g exceeds 0.3
$z^{\max}$	Depth of peak J_q in MI layer
S, $S^{\max}$, S^b	Shear profile, shear at $z^{\max}$ and depth-averaged bulk shear
Q_t	Horizontally averaged turbulent heat flux profile
ϵ	Horizontally averaged dissipation rate profile
ε	Horizontally averaged and daily averaged dissipation rate profile
J_q, $J_{q,p}$	Daily averaged turbulent heat flux profile from LES and parameterizations
$\varepsilon^{\max}$, $\varepsilon_p^{\max}$	Dissipation rate at $z^{\max}$ from LES and its parameterized value
$\gamma_\varepsilon^{\max}$	Dissipation rate normalized by $u_*^2 S^{\max}$
$J_q^{\max}$, $J_q^{\rm MLD}$	Heat flux at $z^{\max}$ and MLD
$J_{q,p}^{\max}$, $J_{q,p}^{\rm MLD}$	Parameterized heat flux at $z^{\max}$ and MLD
$\overline{J}_{q,p}^{\max}$	Depth-averaged parameterized heat flux over the MI layer

We address the questions posed above regarding the DCT response at turbulence time scales and the role of convection in section 3. The third question is answered in the affirmative and a new parameterization for daily averaged subsurface heat flux is introduced in section 4. We then apply the parameterization in the context of the seasonal cycle of the heat flux using the long-time data record from the 0°, 140°W TAO mooring in section 5. Discussion and conclusions are given in section 6.

2. Model setup

We construct a parametric study to investigate the characteristics of DCT over a wide range of surface forcing and background flow conditions. The parameters of interest include westward surface wind stress (τ_w), nighttime convective flux ($Q_{\rm ns}$), shear (S), and the thickness ($h_{\rm MI}$) of the MI layer. The sign convention for the surface heat flux is positive when downward into the ocean. Here, $h_{\rm MI}$ is calculated as the distance between the MLD and the depth where $\mathrm{Ri}_g = N^2/S^2 = 0.3$. Table 1 lists these parameters and some other quantities relevant to our study. For each parameter, we select values from a wide range that was observed during the period between 1990 and 2020 at the 0°, 140°W TAO mooring (Pham et al. 2017). To label the simulations, abbreviation C is used for convection, W for wind, and S and T for the shear and thickness of MI layer, respectively. Increasing numeric labels (1–4 for C, T, and S and 1–6 for W) are used to denote increasing intensity of the forcing in question. The range of values for each parameter is given in Table 2. It should be noted that, in regard to $h_{\rm MI}$, we are specifically interested in how the DCT differs when the MI layer thins during the spring

TABLE 2. Values of surfacing cooling flux (Q_{ns}), initial thickness of MI layer (h_{MI}), wind stress (τ_w), and initial shear magnitude in the MI layer (S_0) used in parametric studies.

Abbreviation	Q_{ns} (W m^{-2})	Abbreviation	h_{MI} (m)	Abbreviation	τ_w (N m^{-2})	Abbreviation	S_0 (s^{-1})
C1	−100	T1	30	W1	−0.005	S1	0.01
C2	−125	T2	40	W2	−0.025	S2	0.015
C3	−150	T3	50	W3	−0.05	S3	0.02
C4	−175	T4	60	W4	−0.075	S4	0.025
				W5	−0.1		
				W6	−0.2		

season. When we vary h_{MI}, T1 refers to the thinnest MI layer (30 m) while T4 indicates the thickest value (60 m). A total of 27 LES cases involving various combinations of forcing parameters are included in the analysis.

The initial zonal current $U(z)$ is modeled after the SEC and the upper flank of the EUC by a three-layer profile: a surface mixed layer ($h_{MLD,0}$ = 25 m) with constant velocity, a MI layer with thickness h_{MI} having constant shear, and a deep layer with constant velocity. The three layers are separated by smooth transitions over a vertical length scale h_{tr} = 8 m. The profile is constructed using the following expression:

$$U(z) = \frac{-h_{MI}S_0}{2} + \frac{h_{tr}S_0}{2}\log\left\{\frac{\cosh[(z + h_{MLD,0})/h_{tr}]/\cosh(h_{MLD,0}/h_{tr})}{\cosh[(z + h_{MLD,0} + h_{MI})/h_{tr}]/\cosh[(h_{MLD,0} + h_{MI})/h_{tr}]}\right\}, \quad (1)$$

where S_0 and h_{MI} are peak shear magnitude and thickness of the MI layer, respectively. The values of S_0 and h_{MI} are listed in Table 2.

Similarly, the initial temperature profile $T(z)$ is modeled with a three-layer profile as follows:

$$T(z) = T_0 + \frac{N_d^2 z}{2\alpha g} - \frac{N_{MI}^2 h_{tr}}{2\alpha g}\log\left\{\frac{\cosh(z + h_{MLD,0})/h_{tr}}{\cosh(h_{MLD,0}/h_{tr})}\right\} + \frac{(N_{MI}^2 - N_d^2)h_{tr}}{2\alpha g}\log\left\{\frac{\cosh[(z + h_{MLD,0} + h_{MI})/h_{tr}]}{\cosh[(h_{MLD,0} + h_{MI})/h_{tr}]}\right\}, \quad (2)$$

where T_0 is a reference temperature, $\alpha = 2 \times 10^{-4}\,°C^{-1}$ is the coefficient of thermal expansion, and g = 9.81 m s^{-2} is gravity. Stratification in the MI layer (N_{MI}^2) is set to be equal $S_0^2/4$ as per the marginal instability condition described above and $N_d^2 = 4 \times 10^{-4}\,s^{-2}$ is the stratification in the deep layer below.

Profiles of zonal current, temperature, squared shear, squared buoyancy frequency, and gradient Richardson number are shown in Figs. 1a and 1b. Since the intensity of the DCT is anticipated to vary with surface heat flux (equivalently surface buoyancy flux B_0) and the product of $u_*^2 S^{max}$, where S^{max} is the shear where the turbulent heat flux peaks in the MI layer, the LES is expected to deliver a wide range of dissipation rates. Figure 1c illustrates the range spanned by the 27 simulations in B_0–$u_*^2 S^{max}$ space. The simulations span two orders of magnitude in terms of $u_*^2 S^{max}$, which provides sufficient data to examine the turbulence scalings. In the present study, initial conditions (i.e., uniform shear and stratification) are idealized to reduce the numbers of parameters involved in the turbulent parameterization analysis. We also exclude large-scale forcing terms such as lateral advection that were considered in W22 as well as in previous LES studies of Wang et al. (1998) and Large and Gent (1999). In the case of Langmuir turbulence, Pearson et al. (2015) found the dissipation rate in the ocean surface boundary layer depends on ML depth. The influence of $h_{MLD,0}$ and other secondary parameters such as h_{tr} is not evaluated here since the number of LES cases is already large.

In each simulation, there is a spinup period in which the ML responds to the applied wind stress. The duration of spinup varies among the cases depending on surface forcing. We allow the ML to develop until peak entrainment (negative) buoyancy flux reaches 25-m depth. After spinup, we reset time to zero and continue the simulations for 24 h. The surface fluxes, i.e., the wind stress and nighttime buoyancy flux, are turned off after the first 12 h such that the surface mixed layer becomes quiescent during the final 12 h, which corresponds to the daytime period. Previous studies have suggested formation of a diurnal warm layer (DWL) during weak wind conditions (Hughes et al. 2020a,b, 2021). Resolving the DWL requires finer grid resolution near the surface which in turn significantly elevates computational cost. Based on our previous studies (Pham et al. 2017; Sarkar and Pham 2019), the turbulent heat flux driven by the DWL occurs at shallow depths during late afternoons and is distinct from our subject of interest—the nighttime DCT in the MI layer. Therefore, to control the computational cost of the LES suite of 27 simulations, we exclude daytime warming from our examination of DCT.

The LES model is based on the Navier–Stokes equations under the Boussinesq approximation for the evolution of velocity components, dynamical pressure, and temperature. The solver uses second-order finite-difference method for spatial derivatives and mixed third-order Runge–Kutta and Crank–

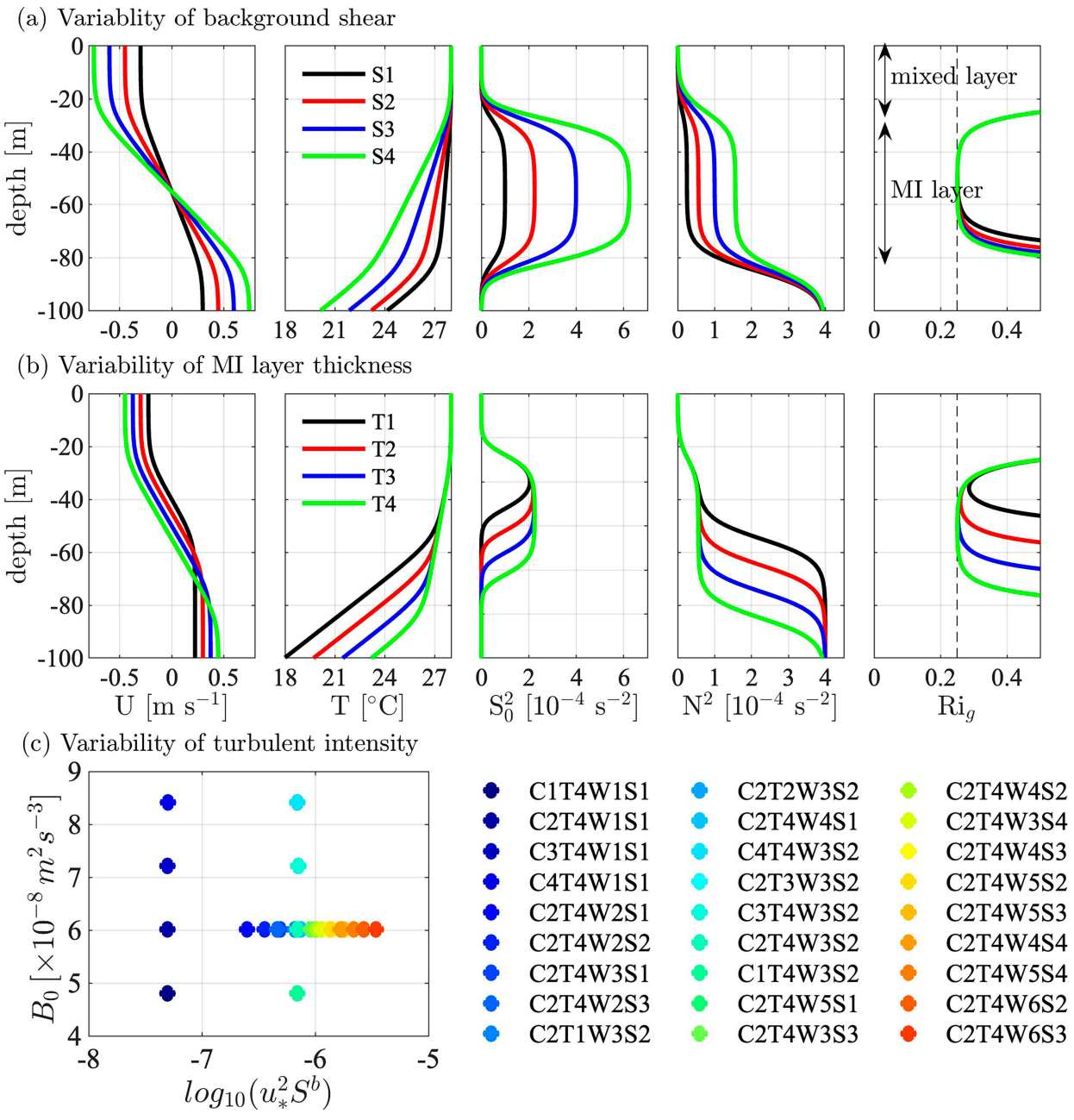

FIG. 1. Initial background profiles used in the parametric study of (a) shear and (b) thickness of MI layer. The panels from left to right show the zonal current (U), temperature difference from a reference value ($T - T_0$), squared shear rate (S^2), squared buoyancy frequency (N^2), and gradient Richardson number (Ri_g). (a) Profiles with variable shear in the DCL: S_0 = 0.01 (black), 0.015 (red), 0.02 (blue), 0.025 (green) s^{-1} and (b) profiles with variable thickness of the DCL: h_{MI} = 30 (black), 40 (red), 50 (blue), 60 (green) m. Black dashed lines on the far right panel mark the critical value of 0.25 for linear shear instability. (c) The wide range of the turbulent energetics in the 27 simulations in the B_0–$u_*^2 S^b$ parameter space.

Nicolson methods for time advancement. A multigrid method is used to solve the Poisson equation for the pressure. The parameterization for LES subgrid stresses utilizes the filter structure function as described by Ducros et al. (1996). A subgrid Prandtl number of unity is assumed to compute the subgrid heat fluxes. Further details of the LES implementation can be found in Pham et al. (2023). We assume that stratification is dominated by the temperature gradient, and thus, we neglect the transport equation for salinity [see supplemental information in Smyth and Moum (2013)]. The effects of Langmuir turbulence and precipitation, which were included by Pham et al. (2023), are also neglected. Rain can impact mixing

in the ocean surface layer (Smyth et al. 1997; Thompson et al. 2019; Moulin et al. 2021) and particularly at the TAO mooring (Whitt 2022). Like DWL, resolving rain layers in LES greatly increases computational cost, and thus, we do not include effects of rain in the present study.

The computational domain is a rectangular box with size of 384 m × 96 m × 143 m in the zonal (x), meridional (y), and vertical (z) direction, respectively. The grid size of 384 × 96 × 384 points in the three directions gives 1-m resolution in the horizontal direction. Vertical resolution is 0.25 m in the upper 90 m and the grid is mildly stretched at 3% below. Periodicity is imposed in the horizontal directions. Wind stress and buoyancy flux are applied at the top surface. A free-slip condition with constant temperature gradient is applied at the bottom surface. A sponge layer is included in the bottom 20 m to prevent the reflection of internal waves.

To diagnose DCT, we examine the evolution of mean and turbulence statistics. Reynolds averages are denoted by angle brackets ($\langle\cdot\rangle$), which are obtained by computing horizontal averages. Turbulence statistics are obtained as averages of quantities involving fluctuations from the mean, which are denoted by primes. Turbulence quantities of primary interest are the turbulent heat flux (Q_t) and the terms in the turbulent kinetic energy (TKE) budget. The heat flux Q_t is obtained by computing the sum of resolved and subgrid heat fluxes $\rho_0 c_p \langle T'w' \rangle + Q_{3,\mathrm{sgs}}$. The major source of the TKE is the shear production $\mathrm{SP} = -\langle u'w' \rangle \partial\langle u \rangle/\partial z$ while the largest sink is dissipation $\epsilon = -\langle \tau'_{ij} s'_{ij} \rangle + 2\nu \langle s'_{ij} s'_{ij} \rangle$, where τ'_{ij} and s'_{ij} are the fluctuating subgrid stresses and fluctuating resolved strain components, respectively. It is noted that the buoyancy flux B is directly related to the heat flux $B = (\alpha g/\rho_0 c_p) Q_t$. Here, $\rho_0 = 1020\ \mathrm{kg\ m^{-3}}$, $\nu = 10^{-6}\ \mathrm{m^2\ s^{-1}}$, and $c_p = 4000\ \mathrm{J\ kg^{-1}\ K^{-1}}$ are reference density, viscosity, and specific heat of seawater, respectively. When we characterize the DCT in terms of daily averages, we will use J_q to denote daily averaged values of Q_t, J_b for the daily averaged B, ε for the daily averaged ϵ, and P for daily averaged SP.

In the present model setup, the ML and MI layers are idealized regimes where turbulence is energized by surface fluxes and by mean shear, respectively. Although they are never realized precisely in the real ocean, these idealizations provide a useful conceptual picture and a guide for parameterizations. Turbulence in the MI layer is modulated by the surface momentum flux, but it is nevertheless distinct from ML turbulence because its primary energy source is the mean shear in the upper flank of the EUC. This mean shear is not directly set by the local wind and upper-ocean stratification, but rather depends on the equatorial ocean dynamics that occurs at larger spatial and temporal scales. This is the key distinction from the parameterization of turbulence in the mixed layer, in which only the local surface forcing and mixed layer depth are required (Pearson et al. 2015). The ML base that separates the ML and MI regimes is defined in the present study by a temperature drop of 0.04 K from the shallowest value (equivalent to a density drop of 0.01 kg m^{-3}). The MI layer is taken to extend from the MLD to the lowermost depth at which $\mathrm{Ri}_g \le 0.3$. While never exact, these criteria are standard in the interpretation of observations and are used here for consistency with the existing literature.

3. Characteristics of nighttime deep-cycle turbulence

Nighttime DCT occurs in multiple bursts during which the instantaneous dissipation rate (ϵ) varies significantly in time and takes values much larger than inside the mixed layer (M89; Smyth et al. 2013; Pham et al. 2013; W22). Vertical profiles of ϵ show a local peak inside the MI layer below which ϵ decreases smoothly until the capping depth where Ri_g increases sharply. In this section, we examine how the forcing parameters affect the bursts of DCT with particular attention to the intensities and vertical distributions of ϵ and Q_t.

a. *Effects of nighttime convection*

It is of interest to examine the role of the convective flux in the cases where the wind stress and the shear are weak and B_0 is comparable to the product $u_*^2 S$. Figure 2 contrasts the evolution of the DCT in the four cases where the intensity of surface cooling is increased from $Q_{\mathrm{ns}} = -100$ to $-175\ \mathrm{W\ m^{-2}}$ (C1–C4) as wind and shear are kept at low values $\tau_w = -0.005\ \mathrm{N\ m^{-2}}$ (W1) and $S_0 = 0.01\ \mathrm{s^{-1}}$ (S1), respectively. Mixed layer depth (MLD) is identified by a temperature decrease of 0.04 K from its value at 5-m depth. Despite weak wind and shear in all cases, DCT occurs and leads to elevated ϵ below the MLD (see magenta lines on left panels in Fig. 2). The main difference among the cases is in the transient behavior of turbulence bursts. Dissipation below the MLD in cases C3 and C4 occurs in pulses while cases C1 and C2 show a more steady evolution that persists throughout the night. The amplitude of the DCT pulsation increases when B_0 increases as previously suggested in Smyth et al. (2017). When averaged over the 24-h period (see red curve in the rightmost panels of Fig. 2), increasing B_0 results in higher values of Q_t.

b. *Effects of initial MI-layer thickness*

We now consider the impacts of increasing h_{MI} from 30 to 60 m (T1–T4) in the left column of Fig. 3. In cases T1–T3, the second burst persists for a significantly longer time than the first. In contrast, the two bursts in case T4 persist for a similar amount of time. The bursts extend to greater depth in cases with thicker initial h_{MI}. Furthermore, the second burst extends deeper than the first burst and peak values of ϵ during the second burst tends to be stronger. Due to entrainment during the first burst, the instantaneous h_{MI} thickens during the second burst, and the thicker MI layer allows the burst to extend deeper into the thermocline.

Peak values of J_q ($-84\ \mathrm{W\ m^{-2}}$ in T2 and $-126\ \mathrm{W\ m^{-2}}$ in T4) tend to increase with increasing h_{MI} although the difference between cases T2 and T3 is minimal. The peak value of daily averaged shear (S) in case T4 is considerably smaller than in the other three cases (see second column of Fig. 3). However, the T4 case has the largest bulk shear computed as an average over the MI layer. This suggests that the peak value of J_q does not increase with the peak value of S in the MI layer, but rather, correlates with the shear at the peak J_q.

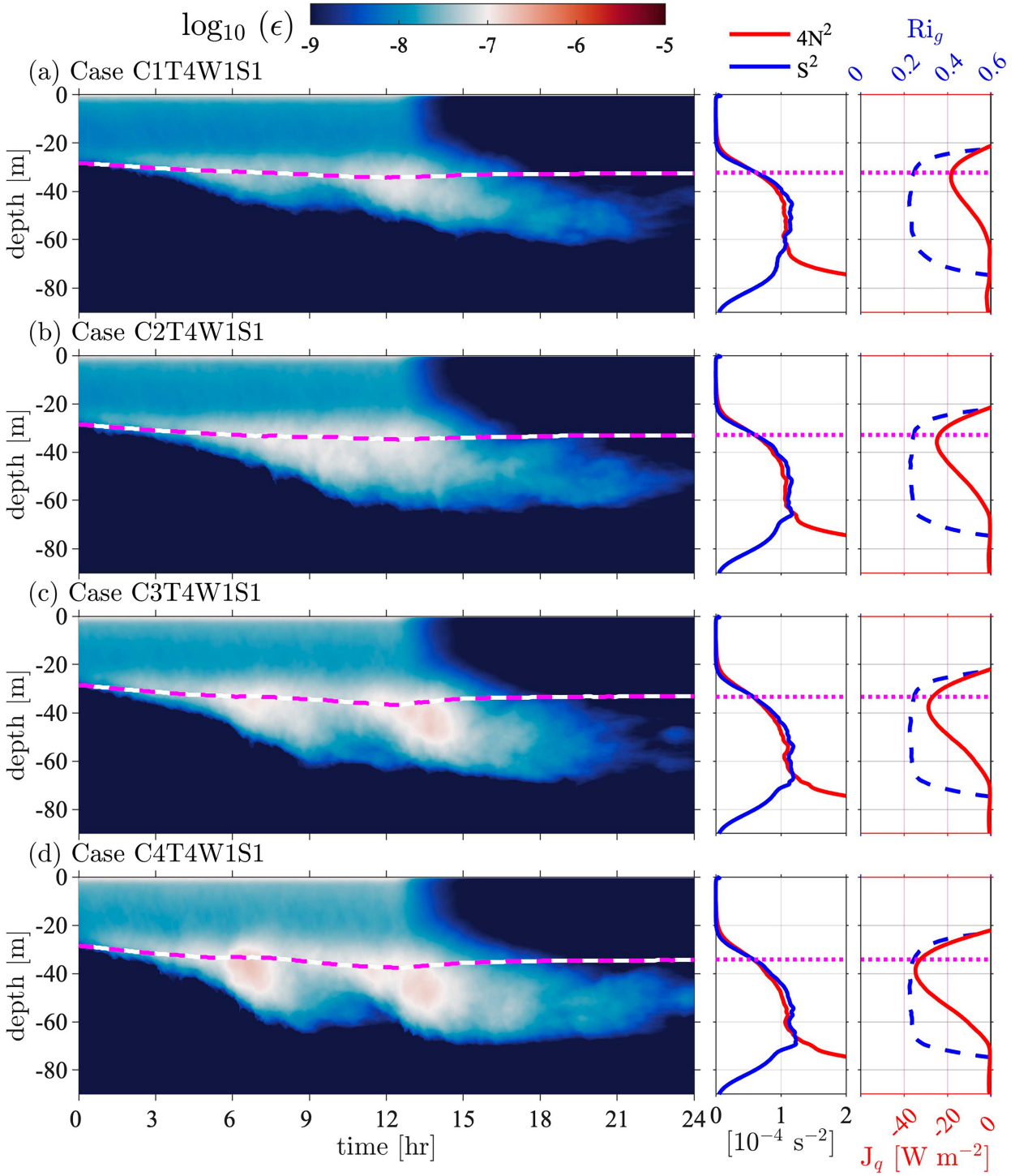

FIG. 2. (a)–(d) Comparison of deep-cycle turbulence among four cases with increasing convection (C1–C4): (left) turbulent dissipation rate, (center) daily averaged profiles of squared shear (S^2) and stratification N^2, and (right) daily averaged profiles of gradient Richardson number (Ri_g) and turbulent heat flux (J_q). The nighttime cooling flux takes the values of 100, 125, 150, and 175 W m^{-2} in the four cases in (a)–(d), respectively. Dashed magenta lines indicate MLD.

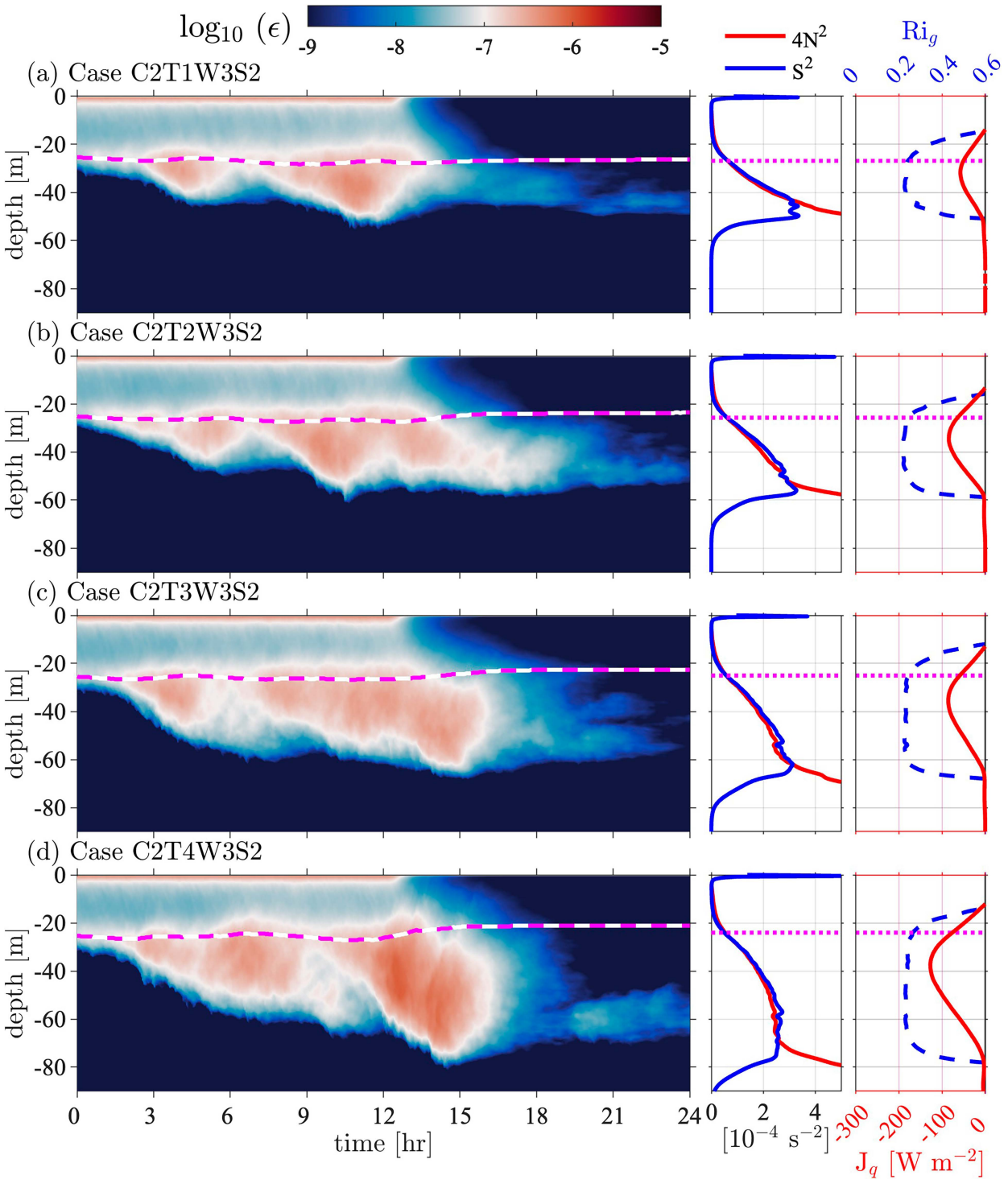

FIG. 3. As in Fig. 2, but among the four cases with increasing MI layer thickness (T1–T4). The MI layer thickness takes the values of 30, 40, 50, and 60 m in the four cases in (a)–(d), respectively.

c. *Effects of wind stress*

Increasing the magnitude of wind stress from $\tau_w = -0.025$ to -0.2 N m^{-2} (W2–W5) intensifies the DCT. The peak value of ϵ is weakest in the W2 case and strongest in the W5 case (see left column in Fig. 4). More importantly, the turbulence occupies the DCL over a longer time period with increasing wind stress. Only one relatively short burst occurs in the W2 case while there are two bursts in the other three cases

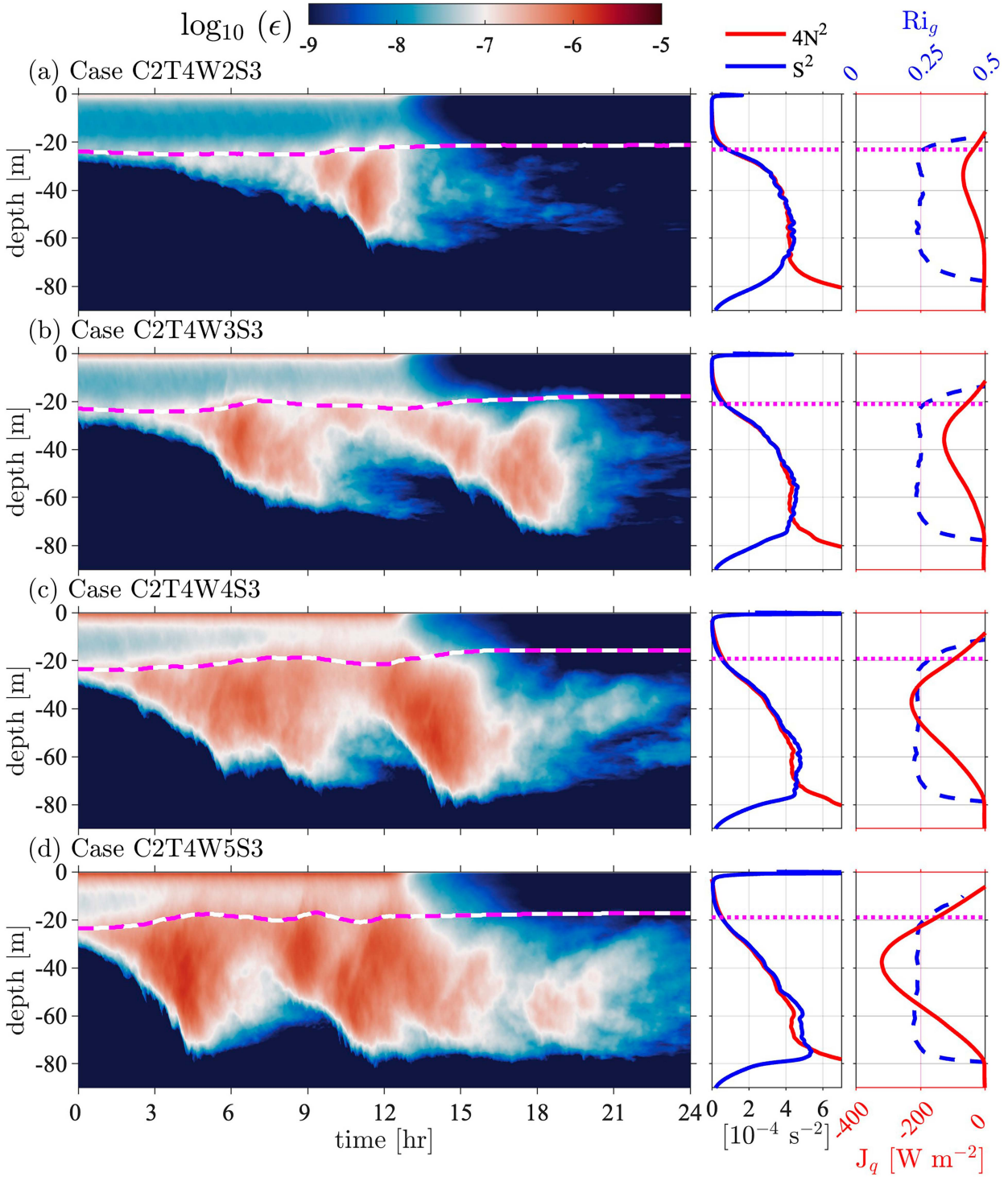

FIG. 4. As in Fig. 2, but among the four cases with increasing wind stress (W2–W5). The wind stress magnitude takes the values of 0.025, 0.05, 0.075, and 0.1 N m^{-2} in the four cases in (a)–(d), respectively, while the shear in the MI layer is held constant at $S = 0.02\ s^{-1}$ (S3).

(noting that we do not count the small pulse occurring at 18 h in the W5 case as a separate burst). Previous studies have suggested that the first DCT burst of the night is triggered by a descending shear layer from the surface mixed layer (Price et al. 1986; Smyth et al. 2013; Pham et al. 2013, 2017). The descending shear layer was found to form in late afternoon when the solar heat flux relaxes. In the present study, we also observe the formation of a shear layer (not shown) at the

MLD prior to the DCT bursts. It deepens into the MI layer and triggers the bursts.

As the wind stress increases from W2 to W5, the first burst occurs at progressively earlier time. In case W2, it takes nearly 9 h for the descending shear layer to penetrate into the DCL and trigger the turbulent burst compared to about 2 h in case W5. Thus, the descent rate of the shear layer is controlled by the wind stress, i.e., the entrainment rate u_e of the descending shear layer correlates with the friction velocity u_*. If the first DCT burst occurs at an earlier time, it is more likely that the night accommodates multiple bursts. Since the initial burst in case W2 occurs late, by the time DCT from that burst has subsided, the night has ended. The convective turbulence has diminished at this time, thus shutting down the trigger mechanism (i.e., the descending shear layer). In contrast, the first burst in case W3 occurs at an earlier time and dissipates at approximately 10 h when the ML turbulence is still sufficiently strong to trigger a second burst.

Increasing τ_w results in stronger daily averaged heat flux (see third column in Fig. 4). The peak value of J_q increases substantially with increasing wind stress. Furthermore, the vertical extent of the J_q profile in case W2 is notably thinner than in the other three cases. When the DCT is relatively weak as in case W2, the turbulent heat flux profile does not spread over the entire vertical extent of the MI layer. In the other three cases, the heat flux diminishes only at depths where Ri_g exceeds 0.25 below the MI layer.

d. *Effects of the MI-layer shear*

Increasing shear in the MI layer also results in stronger DCT (see first column in Fig. 5). The peak value of ϵ increases from S1 to S4 cases. In case S1, one long burst of DCT persists throughout the night. In case S2, weak high-frequency modulation is evident. Cases S3 and S4 show two bursts with significant high-frequency modulation. Since the value of Ri_g in the MI layer is set initially to 0.25 in all cases, the initial buoyancy frequency (N) increases proportionally to the initial shear. Increasing N and S among these four cases promotes growth and modulation of DCT. Due to the increase of DCT with increasing MI-layer shear, the daily averaged MLD becomes shallower (by almost 14 m from S1 to S4). Peak values of J_q are larger with increasing shear (see second and third columns in Fig. 5).

The peak values of J_q are similarly large in the high-shear S4 case of this series and the high-wind W5 case of the wind stress variation series. However, there is a difference in the DCT profiles. As noted above, large MI-layer shear tends to spread the DCT turbulence upward and shallows the mixed layer (by about 14 m from S1 to S4). Increasing wind (cf. W5 to W2 in the rightmost panel of Fig. 4) has little effect on the daily average MLD.

While DCT is enhanced when MI-layer shear is increased (i.e., Fig. 5), τ_w also contributes to increased turbulent mixing (i.e., Fig. 4). The dependence of DCT on both S and τ_w highlights unique characteristics of forced MI and the resulting DCT. The MI state represents more than just a local (to the EUC) shear instability because the triggering mechanism is as important as the local shear with respect to turbulence energetics. For instance, the entrainment rate of the descending shear layer depends on the wind stress and correlates with DCT and its heat transport as was illustrated in section 3c. Furthermore, the instantaneous dissipation induced by DCT is influenced by the shear and stratification local to the MI layer. The stronger is the shear in the MI layer, the stronger is the DCT. These characteristics of MI and DCT further confirm that the parameterization of ε requires taking into account the strength of surface processes (e.g., wind stress and convection) as well as of the local EUC shear (S21; W22). MI is not unique to the Pacific equatorial ocean. It has also been observed in other oceanic settings such as in Columbia River plume and Mediterranean outflow where the control parameters are different from the ones being considered in the present study (Smyth 2020). Recent laboratory experiments on stratified inclined duct flows (Lefauve et al. 2019) and simulations of forced stratified shear layers (Smith et al. 2021) also show the occurrence of MI in these idealized flow problems. Those studies suggested that the parameterization of the turbulent mixing driven by MI requires a more exhaustive list of control parameters.

e. *Nonmonotonic behavior of J_q*

While we attempt to extract the DCT dependence on the different forcing parameters in the discussion above, it should be noted that the dependence exhibits variability due to the multiple physical effects involved. This is especially true of the transient behavior of the DCT. The number of turbulent bursts, the peak dissipation in each burst and the persistence of each burst control the net amount of mixing in the DCL over the daily time scale. Figure 6 contrasts J_q in six separate groups. In each, we focus on the correlation between J_q and a particular forcing parameter. Nonmonotonic behavior is observed when the MI layer thickness is varied. The peak value of J_q does not increase between the T2 and T3 cases (i.e., Fig. 6b). In the two groups where we vary τ_w while holding S in the MI layer constant at S2 and S3 (i.e., Figs. 6c,d, respectively), there is monotonic increase in the peak value of J_q with increasing τ_w. The monotonic increase is also observed in the group in which S increases while holding τ_w constant at W3 (i.e., Fig. 6f). However, when we vary S at W3 wind, the peak values of J_q are similar between cases S2 and S3 (i.e., Fig. 6e). The nonmonotonic behavior in the relationship between J_q and the forcing parameters exhibited in some of the groups poses challenges in the parameterization of DCT. Furthermore, since turbulence is a chaotic dynamical system, the bursts of DCT can be sensitive to small perturbations of the background flow and the surface forcing (Liu et al. 2022). Nevertheless, within the parameter space of the present study (which is representative of conditions observed in the Pacific equatorial ocean), we see generally larger J_q in cases with larger τ_w and S (i.e., Figs. 6c,d,f). Thus, we are able to identify from the LES that τ_w and S_0 have stronger influence on turbulent heat flux than Q_{ns} and h_{MI}, similar to the results found in S21 and W22.

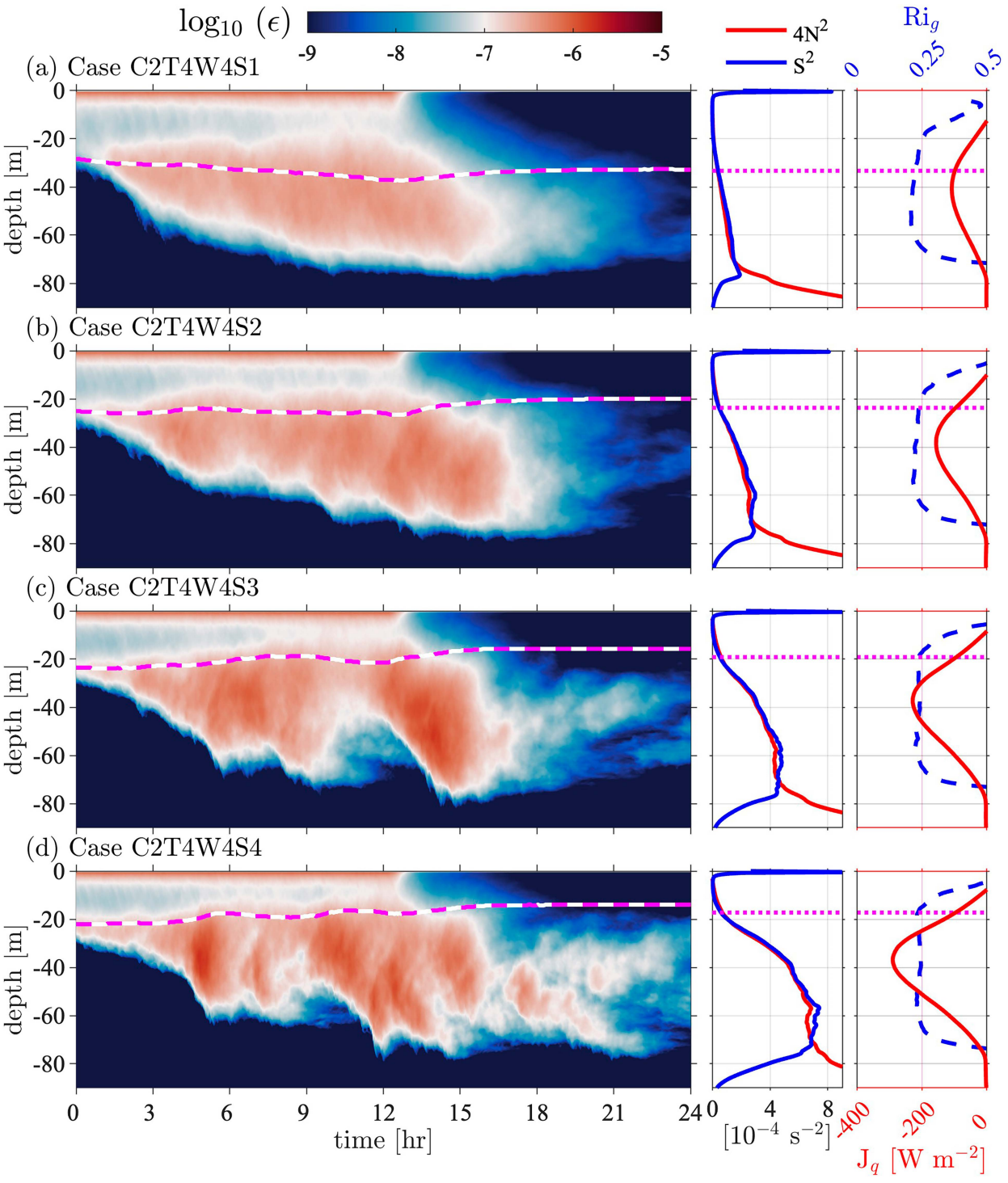

FIG. 5. As in Fig. 2, but among the four cases with increasing shear in the MI layer. The shear (S_0) takes the values of 0.05, 0.1, 0.15, and 0.2 s^{-1} in the four cases in (a)–(d), respectively while the wind is held constant at $\tau_w = -0.075$ N m^{-2} (W4).

4. Parameterization of daily averaged deep-cycle turbulence

As the forcing parameters (i.e., Q_{ns}, h_{MI}, τ_w, and S) are varied in control simulations as discussed in the previous section, we observe the following trends in the DCT and the resulting daily averaged heat flux (J_q):

1) The intensity of J_q, especially at its larger values, is mostly influenced by τ_w and S. Increasing Q_{ns} and h_{MI}

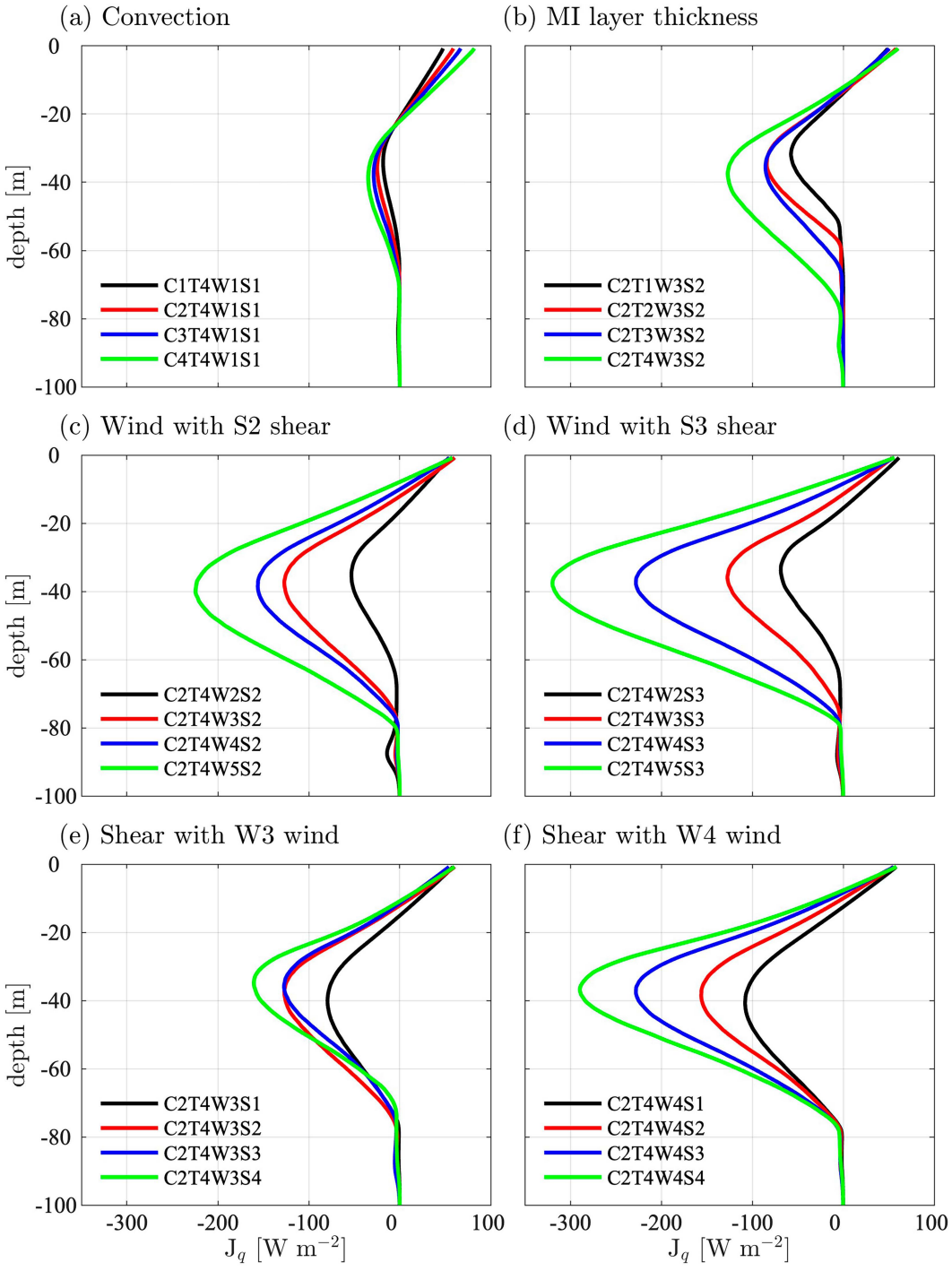

FIG. 6. Comparison of daily averaged turbulent heat fluxes in various parametric studies: (a) convection, (b) MI layer thickness, (c) wind with moderate shear (S2), (d) wind with strong shear (S3), (e) shear with moderate wind (W3), and (f) shear with strong wind (W4).

to high observed values also enhances the DCT but less strongly.

2) While there is a correlation between the MI-layer shear S and the intensity of J_q, peak values of J_q do not occur at the depth with the strongest shear.
3) The intensification of J_q occurs continuously from the surface to the base of the MI layer.
4) Once DCT occurs (e.g., as in Figs. 2–5), the dissipation rate ε tends to increase rapidly relative to the region above the MLD. Thus, the MLD can be used to

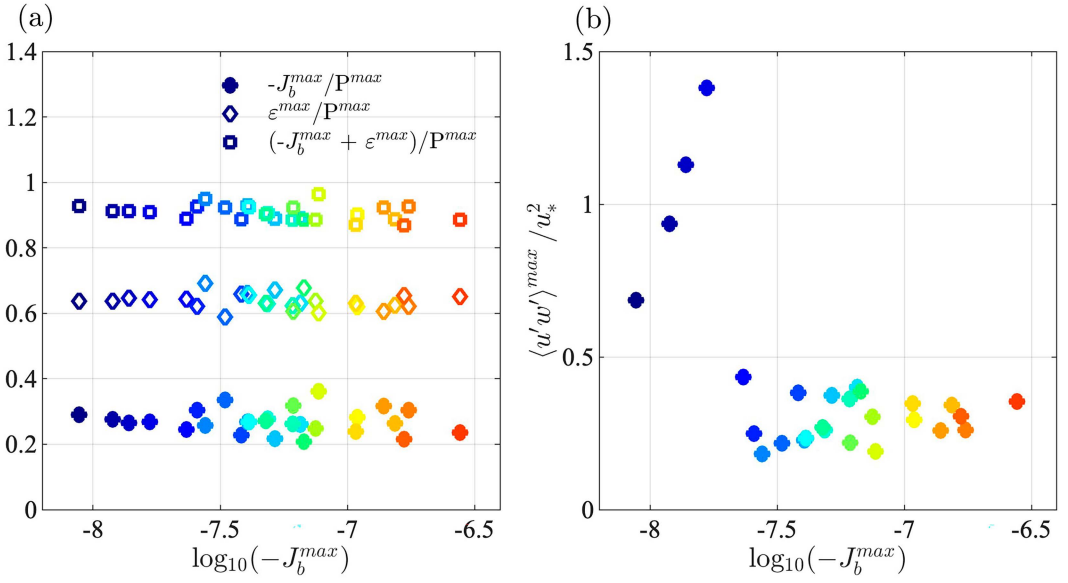

FIG. 7. (a) Energetics at $z^{\max}$ indicates the dominant balance between the daily averaged turbulent production ($P^{\max}$), dissipation ($\varepsilon^{\max}$) and buoyancy flux ($J_b^{\max}$). (b) The momentum flux J_m at $z^{\max}$ is directly proportional to the wind stress (i.e., u_*^2) in the strong turbulence regime where $-J_b^{\max} \geq 10^{-7.8}\,\mathrm{m^2\,s^{-3}}$. Marker colors denote different cases as previously defined in Fig. 1.

set the upper bound on the vertical extent of the $J_q(z)$ profile.

Based on these observations, we construct parameterizations for the daily averaged dissipation rate and subsurface turbulent heat flux.

a. Parameterization of ε

To further gain insights to what controls the turbulence in the deep-cycle layer, we analyze the TKE budget at the depth where the turbulent heat flux is most intense (i.e., $z^{\max}$). Figure 7a shows that the local shear production ($P^{\max}$) is the major source of TKE and it is mainly balanced by $\varepsilon^{\max}$ and the buoyancy flux ($J_b^{\max}$). The flux Richardson number ($\mathrm{Ri}_f = -J_b^{\max}/P^{\max}$) varies between 0.21 and 0.38 and the ratio $\varepsilon^{\max}/P^{\max}$ clusters in a range between 0.59 and 0.69 despite the wide variability in $J_b^{\max}$ ($10^{-8} \leq -J_b^{\max} \leq 10^{-6.5}\,\mathrm{m^2 s^{-3}}$, a factor of 32). The values of the ratio $\varepsilon^{\max}/P^{\max}$ and Ri_f in the present LES fall within the range reported in DNS of stratified shear flows (Jacobitz et al. 1997; Smyth et al. 2001; Pham et al. 2009; VanDine et al. 2021).

The similarity suggests that the shear local to the deep-cycle layer is the main source of TKE. To inspect the role of the surface wind stress, Fig. 7b shows how the momentum flux $J_m^{\max}$ at $z_{\max}$ varies with $J_b^{\max}$. In the regime of strong DCT ($-J_b^{\max} \geq 10^{-7.8}\,\mathrm{m^2\,s^{-3}}$), $J_m^{\max} = \langle u'w'\rangle^{\max}$ is directly proportional to u_*^2. However, $J_m^{\max}$ does not follow such proportionality in the regime $-J_b^{\max} < 10^{-7.8}\,\mathrm{m^2\,s^{-3}}$, which suggests that surface convective flux contributes significantly under weak-wind/weak-shear conditions. We note that W22 also identified a transition between two regimes of DCT at a similar value of $J_b^{\max}$ although they did not consider the possible effect of convection in their parameterization.

Overall, the analysis of TKE budgets at $z^{\max}$ indicates that the shear local to the MI layer, wind stress and possibly surface convective flux are the important parameters in the parameterization of ε. To explore how ε varies across the two regimes of mixing (in terms of $J_b^{\max}$), Fig. 8a shows the vertical profiles of ε normalized by $u_*^2 S^{\max}$, where $S^{\max}$ is the shear at $z^{\max}$. The normalized profiles indicate a spread as large as a factor of 10 in terms of peak normalized dissipation rate. Figure 8b reveals how the peak normalized dissipation rate ($\gamma_\varepsilon^{\max} = \varepsilon^{\max}/u_*^2 S^{\max}$) varies with the ratio $u_*^2 S^{\max}/B_0$. In the cases with $u_*^2 S^{\max}/B_0 \geq 4$, $\gamma_\varepsilon^{\max}$ clusters in a narrow range between 0.12 and 0.28. When $u_*^2 S^{\max}/B_0 \leq 4$, however, $\gamma_\varepsilon^{\max}$ increases sharply as $u_*^2 S^{\max}/B_0$ decreases. We perform regression using the following form:

$$\gamma_{\varepsilon,p}^{\max} = a\left(\frac{u_*^2 S^{\max}}{B_0}\right)^{-1} + b, \tag{3}$$

and find the coefficients $a = 0.36$ [0.32, 0.4], $b = 0.18$ [0.15, 0.2], and the correlation coefficient $r^2 = 0.93$. The quantities included in square brackets indicate the 95% confidence interval. This leads to a new parameterization for the peak dissipation rate:

$$\varepsilon_p^{\max} = 0.36 B_0 + 0.18 u_*^2 S^{\max}. \tag{4}$$

Figure 8c shows the vertical profiles of ε again but normalized using the new scaling obtained above. Relative to Fig. 8a, the spread among the profiles is limited within a factor of 2 in terms of peak normalized values.

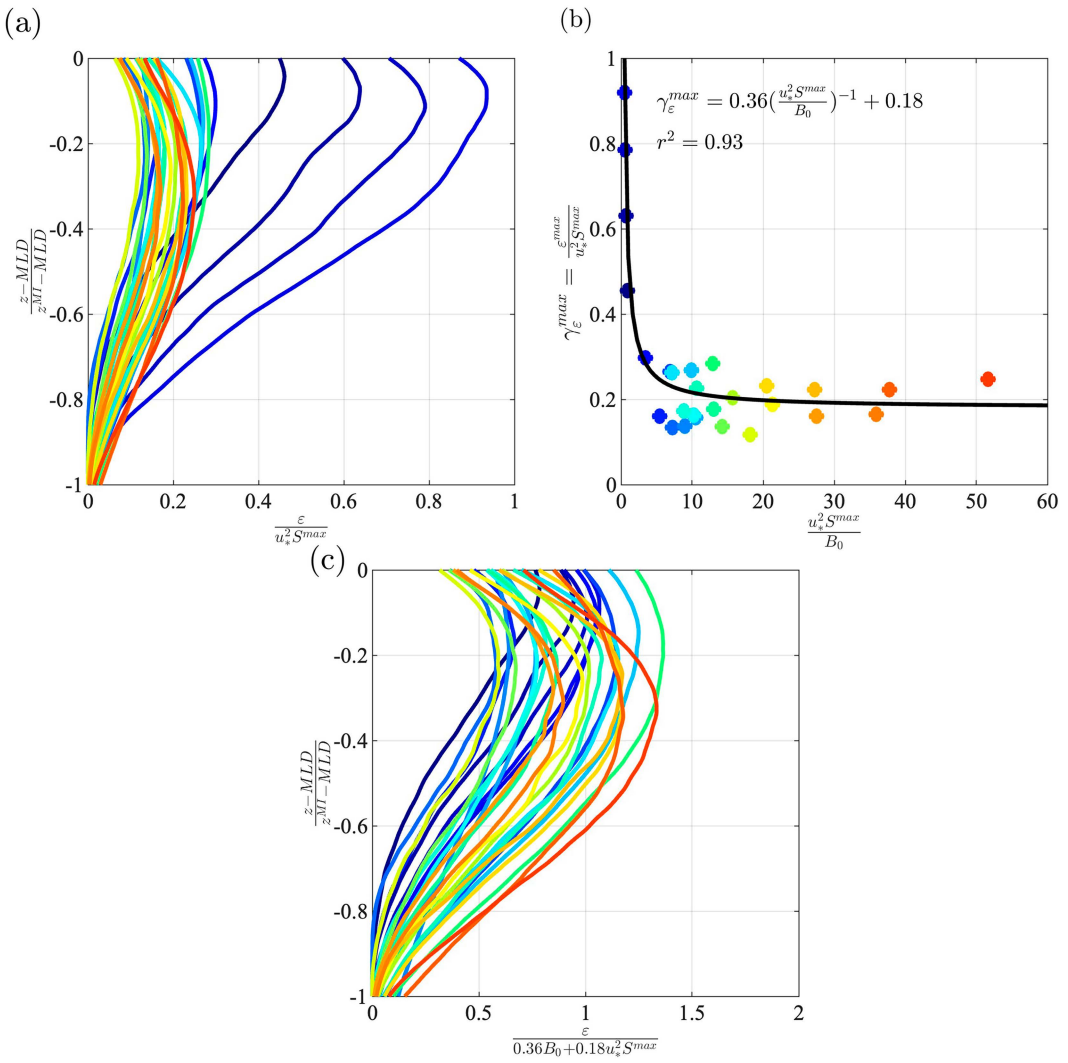

FIG. 8. (a)–(c) Parameterization of daily averaged dissipation rate. Vertical profiles in (a) are normalized by $u_*^2 S^{\max}$. Panel (b) shows a new parameterization for the peak dissipation rates that depend on B_0 and $u_*^2 S^{\max}$. The vertical profiles normalized by the new scaling are shown in (c). The profiles in (a) and (c) are only shown in the MI layer. Marker and line colors denote different simulations as in Fig. 1c.

b. *Parameterization of J_q*

We aim to parameterize the turbulent heat flux profile, $J_{q,p}(z)$, specifically the values of heat flux at three depths: the MLD, the base of the MI layer, and the location of peak J_q at $z = z^{\max}$. These three locations are denoted by the red stars in the schematic diagram in Fig. 9a. Historically, M89 and S21 among other studies of DCT (Lien et al. 1995; Pham et al. 2017) chose to quantify the turbulent mixing in the DCL separately from the turbulence in the mixed layer. Observation 4, discussed at the beginning of this section, also supports the use of MLD as the upper bound of the MI layer. The use of a cutoff gradient Richardson number to set the lower bound of the MI layer (i.e., observation 3 above) is consistent with S21 and W22.

Exclusion of the mixed layer from our DCT parameterization has operational advantages as opposed to W22, who chose to include the mixed layer turbulence in their parameterization. The shear data in the surface mixed layer at the TAO mooring is highly limited while the shear in the MI layer is more readily available. By tuning the control parameters (i.e., shear and stratification) to the MI layer instead of the surface mixed layer, we are able to apply the parameterization to the long-term TAO mooring data as will be demonstrated in the next section. For simplicity and ease of comparison with the relatively coarsely-resolved χ-pod data and as previously done in W22, we assume that $J_{q,p}$ has a piecewise-linear form defined by the values of heat fluxes at these three depths—MLD, $z^{\max}$, and z^{MI}. With respect to the J_q profile from the LES case shown in Fig. 9a, the linear approximation slightly underestimates the heat flux.

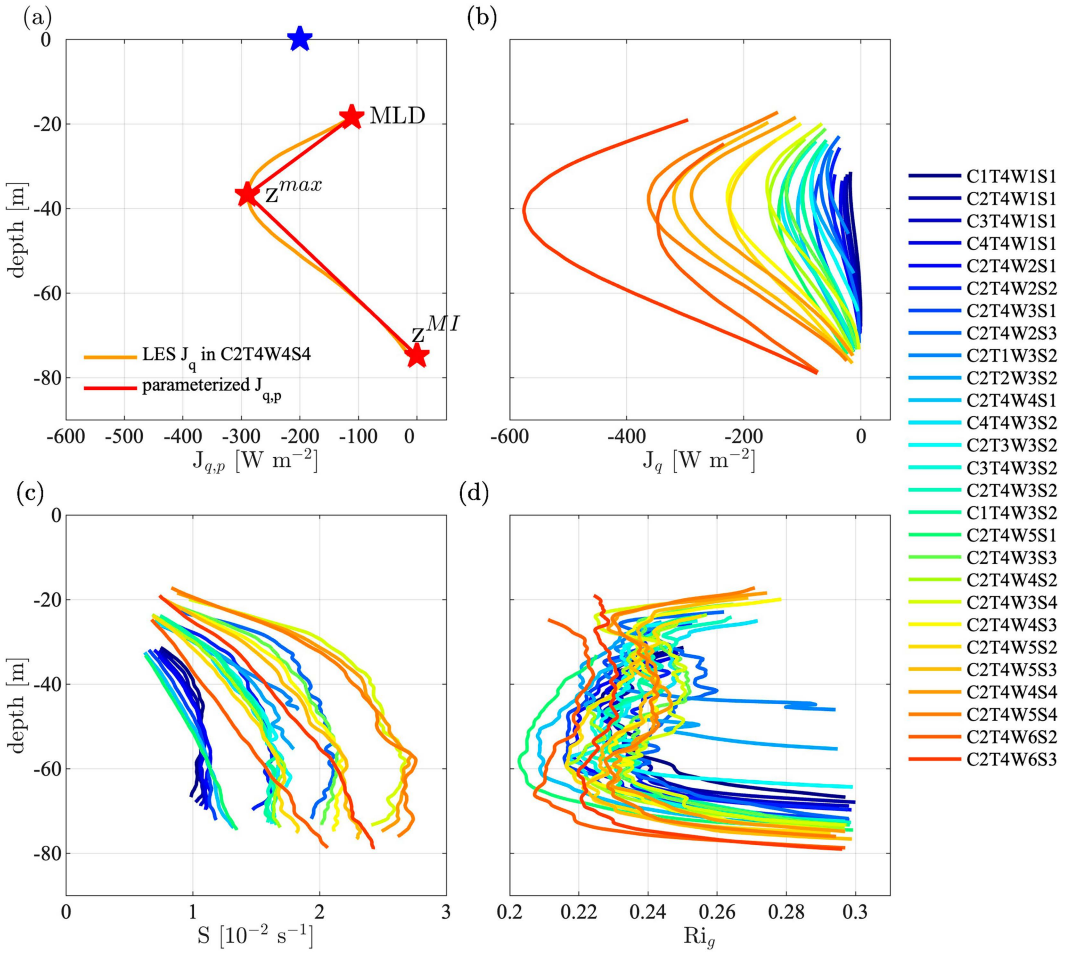

FIG. 9. (a) A schematic for a parameterization of the daily averaged turbulent heat flux profile $J_{q,p}(z)$. The parameterization is constructed using the daily averaged z-dependent profiles of (b) turbulent heat flux (J_q), (c) shear, and (d) gradient Richardson number. The profiles in (b)–(d) only show the values inside the MI layer.

In the rest of this section, we will use the LES suite to find formulae for $z^{\max}$ and z^{MI} and the corresponding values of J_q at these depths as well as at the MLD (the MLD is readily available from the TAO mooring and does not require parameterization). The formulae are deduced based on the daily averaged profiles of J_q, S and Ri_g from the 27 simulations along with the employed surface forcing (see Figs. 9b–d). We emphasize that the parameterization uses *daily averaged* background flow conditions from the LES rather than initial conditions in order to account for intraday evolution of DCT in the LES and its effect on the background. There is no loss of generality since the daily averaged shear across the MI layer spans a range as wide as the initial shear (cf. the shear values in Table 2 and the shear profiles in Fig. 9c).

Motivated by observation 3 that J_q decreases to zero at the base of the MI layer, we select the threshold value of $\mathrm{Ri}_g = 0.3$ to locate z^{MI} and set $J_{q,p}$ to be zero at this depth. Figure 9b, in conjunction with Fig. 9d to determine the location of $\mathrm{Ri}_g = 0.3$, shows J_q values at z^{MI} are smaller than 20 W m^{-2} in nearly all simulations except for the cases with strongest ($W6$) wind. Using a higher value of Ri_g for the threshold deepens the MI layer. Such extension in the vertical, although small, deteriorates the agreement between the parameterization and the χ-pod data due to the large shear at z^{MI} (see Fig. 9c). Including the larger shear would be incorrect since it falls outside the region with significant turbulent heat flux. We note that the parameterization in W22 used a slightly larger value of $\mathrm{Ri}_g = 0.35$ while S21 used $\mathrm{Ri}_g = 0.25$ for z^{MI}.

Taking the cue from observation 1, we aim to deduce the relationship between the parameterized peak heat flux ($J_{q,p}^{\max}$) and the product $u_*^2 S^{\max}$ in the form:

$$J_{q,p}^{\max} = -\gamma_J^{\max} \frac{\rho_0 c_p}{\alpha g} u_*^2 S^{\max}, \tag{5}$$

where the coefficient $\gamma_J^{\max}$ can vary with the ratio $u_*^2 S^{\max}/B_0$ as was observed for the dissipation rate in section 4a. For the maximum heat flux, Fig. 10a indicates

$$\gamma_J^{\max} = a\left(\frac{u_*^2 S^{\max}}{B_0}\right)^{-1} + b, \tag{6}$$

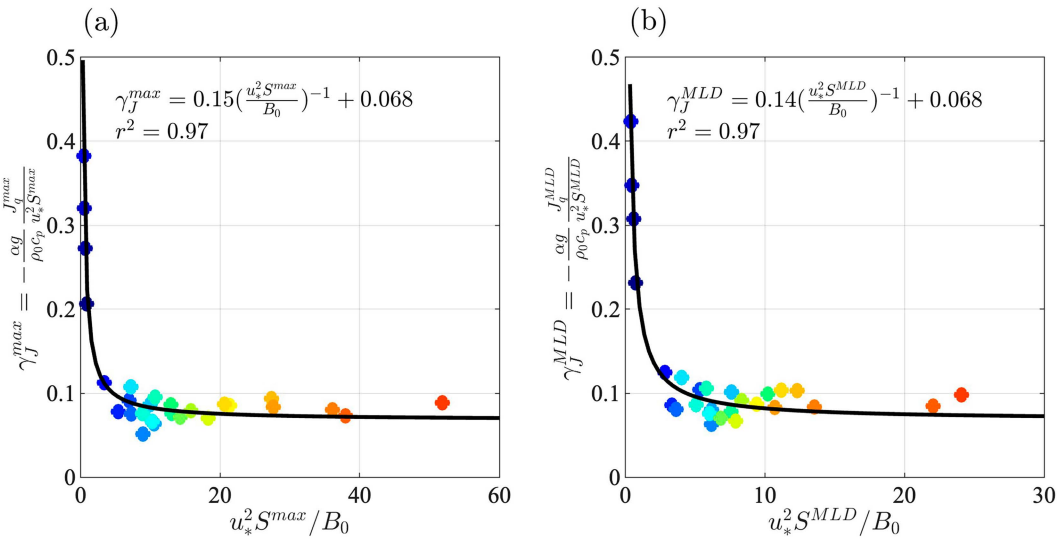

FIG. 10. Parameterization of (a) the peak heat flux ($J_q^{\max}$) and (b) the heat flux at the MLD (J_q^{MLD}). Colors are used to indicate different simulations as in Fig. 1a.

where the coefficients $a = 0.15$ [0.14, 0.16] and $b = 0.068$ [0.061, 0.074] and $r^2 = 0.97$. This leads to

$$J_{q,p}^{\max} = -\frac{\rho_0 c_p}{\alpha g}(0.15B_0 + 0.068u_*^2 S^{\max}). \tag{7}$$

Carrying out the same analysis for the heat flux at the MLD, Fig. 10b indicates that the normalized heat flux (γ_J^{MLD}) varies as follows:

$$\gamma_J^{\mathrm{MLD}} = a\left(\frac{u_*^2 S^{\mathrm{MLD}}}{B_0}\right)^{-1} + b, \tag{8}$$

where the coefficients $a = 0.14$ [0.13, 0.15] and $b = 0.068$ [0.06, 0.076] and $r^2 = 0.97$. This results in

$$J_{q,p}^{\mathrm{MLD}} = -\frac{\rho_0 c_p}{\alpha g}(0.14B_0 + 0.068u_*^2 S^{\mathrm{MLD}}). \tag{9}$$

The scalings of $J_{q,p}^{\mathrm{MLD}}$ and $J_{q,p}^{\max}$ exhibit little difference in the regression coefficients and the correlation coefficients ($r^2 = 0.97$) are the same for the two scalings, suggesting that the local properties of the turbulence are controlled by the local shear rate.

To complete the parameterization of $J_{q,p}(z)$, we formulate a method to deduce the depth $z^{\max}$. Figures 11a and 11b hint at a correlation between $z^{\max}$ and the shear centroid of the MI layer (z^{cen}, defined as the depth where the local shear equals the depth-averaged value S^b). In general, z^{cen} varies similarly as $z^{\max}$ among cases, suggesting that $z^{\max} \propto z^{\mathrm{cen}}$. Since the MI layer is separated from the surface by the ML, we add the contribution of MLD using the following form: $z^{\max} = az^{\mathrm{cen}} + b\mathrm{MLD}$ where a and b are coefficients to be determined. Dividing both sides of the equation by the MLD and performing linear regression reveals the following relationship (see Fig. 11c):

$$\frac{z^{\max}}{\mathrm{MLD}} = a\frac{z^{\mathrm{cen}}}{\mathrm{MLD}} + b, \tag{10}$$

where the coefficients $a = 1$ [0.89, 1.11] and $b = -0.2$ [−0.39, −0.03] and $r^2 = 0.94$. We note that $z^{\max}$, z^{cen}, and MLD take negative values in the present sign convention. Equation (10) can be rewritten in the following form:

$$z^{\max} = z^{\mathrm{cen}} - 0.2\mathrm{MLD}. \tag{11}$$

c. *Summary of J_q parameterization*

We have developed a parameterization of $J_{q,p}(z)$ profile intended to infer the turbulent heat flux from basic field observations that do not include microstructure data. The parameterization permits an estimate of J_q, in the upper-ocean surface layer at 0°, 140°W TAO mooring from the available surface forcing, shear, and stratification data since the beginning of the mooring deployment. The $J_{q,p}(z)$ is a piecewise linear profile that connects the heat fluxes at three locations, signified by the subscript p: z_{MLD} from the observed ML thickness, z_{MI} from the lowest depth where $\mathrm{Ri}_g \le 0.3$ in the observations and, finally, the location, $z^{\max}$, where J_q peaks, given by Eq. (11). The daily averaged profiles of shear and stratification are sufficient to obtain these three locations. The heat flux is zero at z_{MI}, given by Eq. (9) at z_{MLD}, and given by Eq. (7) at $z_{\max}$. Equations (7) and (9) require the wind stress and the shear profile as inputs. Thus, with Eqs. (7), (9), and (11), we have deduced a complete formulation to parameterize $J_{q,p}(z)$ using observed surface forcing and observed shear/stratification profiles.

5. Seasonal cycle of deep-cycle heat fluxes

Previous observational and LES studies have indicated that the DCT exhibits seasonal variability with strong subsurface heat flux during boreal summer months and weaker mixing

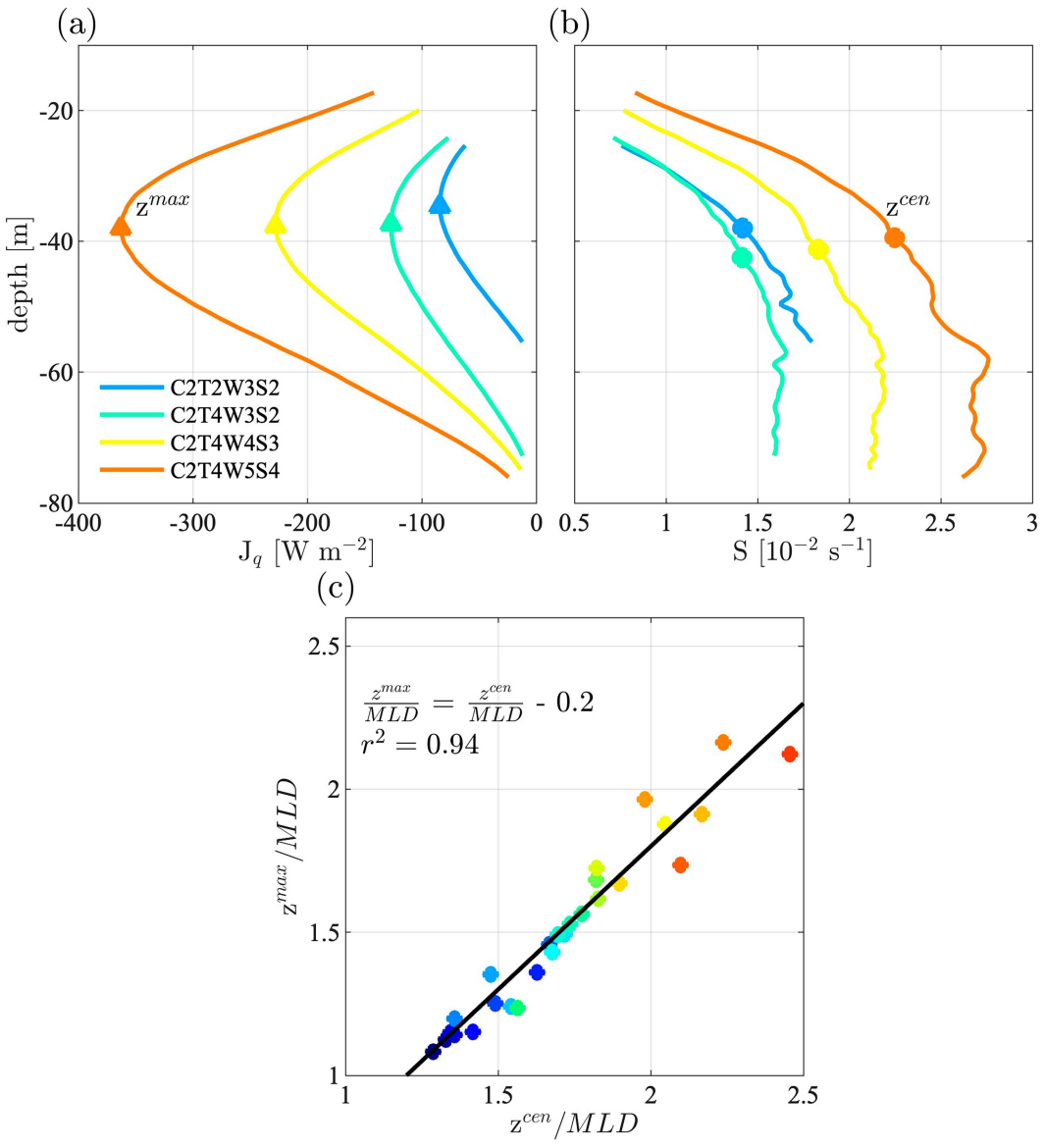

FIG. 11. Parameterization of the depth ($z^{\max}$) with peak J_q: (a) J_q profiles with marked $z^{\max}$, (b) shear profiles with marked centroid (z^{cen}), and (c) scaling of $z^{\max}$ and z^{cen}. Panels (a) and (b) only show four cases for illustrative purposes. The solid line in (c) indicates the best linear fit.

during the spring and autumn (Moum et al. 2013; Pham et al. 2017; Sarkar and Pham 2019). In this section, we apply the heat flux parameterization ($J_{q,p}$) from section 4c to explore its variability in monthly averages. Equations (7), (9), and (11), as summarized in section 4, are used to implement the heat flux parameterization. Using the observed daily averaged profiles of shear and stratification and surface fluxes collected at 0°, 140°W TAO mooring from May 1990 to April 2020, we obtain the parameterized daily averaged heat flux profiles as demonstrated in Fig. 12 for three sample dates. We then bin these daily profiles into the 12 months of the year to deduce the variability of the turbulent heat flux over the seasonal cycle.

Before discussing the seasonal cycle of the turbulent heat flux, we first examine how the surface forcing and background flow conditions change between seasons. Figure 13a shows the observed seasonal variability of solar heat flux Q_s, nonsolar heat flux Q_{ns}, and τ_w [see Pham et al. (2017) for further details]. The wind stress shows small values during boreal spring with a minimum in April. The strongest winds occur in August, then slightly decrease during fall increasing again in winter. The strong peaks in August and December are comparable. The ratio $u_*^2 S^{\max}/B_0$ plotted in Fig. 13b shows a range between 9 and 15 which suggests that τ_w and S are the dominant contributor to the DCT. The contribution of B_0 to the DCT is of order 10% or less in monthly averages (although it

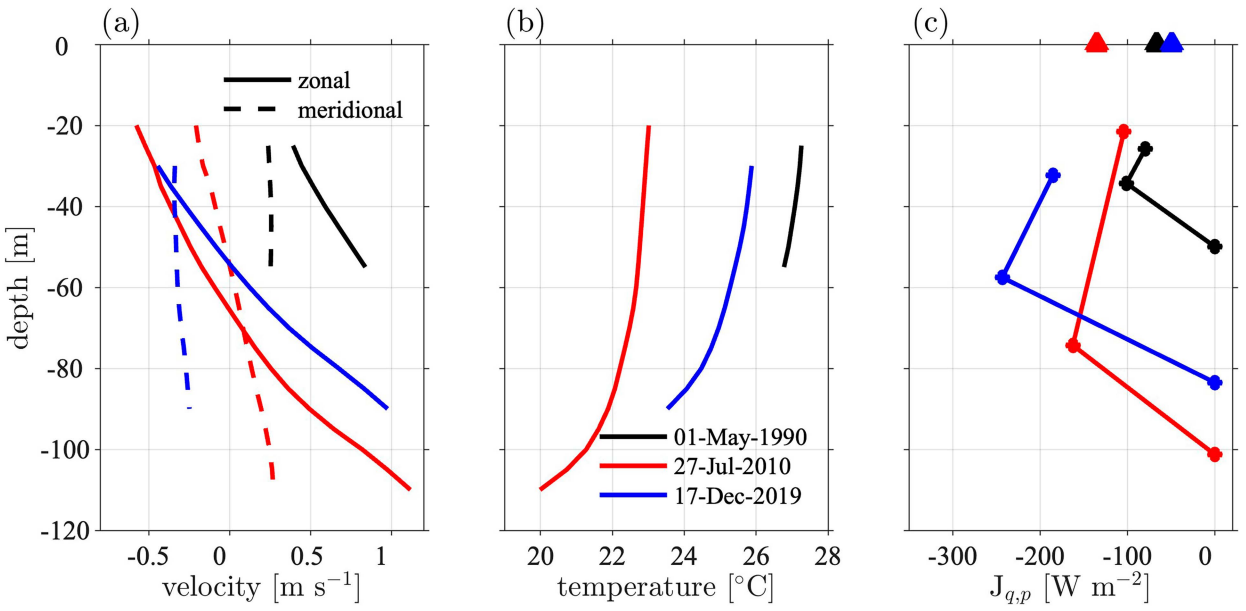

FIG. 12. Parameterization of daily averaged profiles of turbulent heat fluxes: (a) observed zonal (dashed) and meridional (solid) velocities, (b) observed temperature, and (c) parameterized turbulent heat fluxes. The markers at $z = 0$ in (c) denote difference between the net downward surface heat flux $-Q^{\text{net}}$ and the penetrative solar heat flux $I^{\max}$ at $z^{\max}$.

can be significant on days with weak winds and weak shear). Vertical profiles of monthly-averaged shear are shown in Fig. 13c. The MI layer, denoted by solid lines, extends deepest into the EUC core during the winter. Within the MI layer, the shear during the spring is considerably stronger than during the other three seasons. The conditions during the months of April and August are intriguing. The month of April has the strongest shear in the MI layer but the weakest wind of the entire cycle. In contrast, the wind peaks in August while the MI shear is notably smaller than during April. It is of interest to explore how the parameterized heat fluxes differ between these two months and the applicability of $J_q^{\max} \propto u_*^2 S^{\max}$.

From the daily averaged heat flux profiles (samples are shown in Fig. 12c), we obtain the monthly averaged parameterized peak heat flux $J_{q,p}^{\max}$ and its depth $z_p^{\max}$ as shown in Fig. 14a. In general, $J_{q,p}^{\max}$ is weakest in spring and strongest in summer. The heat flux reaches its seasonal minimum value in April when τ_w is weakest. The largest $J_{q,p}^{\max}$ occurs in August, consistent with the strong τ_w during this time period. The heat flux increases by a factor of 2 between April and August. Although τ_w are similar between August and December, $J_{q,p}^{\max}$ is stronger in the former because the shear in the MI layer is relatively stronger at this time. The depth $z_p^{\max}$ shoals to approximately 35-m depth in April and then deepens into the EUC core during summer and fall. The peak heat flux extends deepest to approximately 58-m depth in December.

To compare the parameterized heat flux with the observed heat flux from the χ-pods (available at the TAO mooring from September 2005 to March 2019), we compute the bulk (depth average) parameterized heat flux ($\bar{J}_{q,p}$) by first averaging the daily averaged parameterized heat flux profile over the MI layer and then binning the result into months. The observed heat flux from the χ-pods is available at 29-, 39-, 49-, 59-, 69-, 89-, and 119-m depths, and we use the same averaging method to obtain the annual cycle of J_q. Figure 14b demonstrates reasonable agreement between the seasonal cycle of the parameterized values (red dashed line) and the χ-pod values (black solid line). Both reveal that J_q is strongest in summer and weakest in spring. Over the entire cycle, the parameterized heat flux shows larger values when compared to the observed values except for August. The larger values in the parameterization are possibly due to the greater vertical extend of the MI layer relative to the vertical extent of χ-pod deployments. Figure 13c indicates the top of the MI layer (i.e., MLD) is likely to be shallower than the 30-m depth throughout the cycle, and thus, the large amount of heat flux above this depth was not captured by the χ-pods. The peak heat flux ($J_{q,p}^{\max}$) in Fig. 14a is reduced relative to the bulk heat flux ($\bar{J}_{q,p}$) in Fig. 14b. The peak-to-peak April–August difference in $J_{q,p}^{\max}$ is approximately 86 W m^{-2} while the difference in $\bar{J}_{q,p}$ between the two months is only 55 W m^{-2}. Depth averaging over MI layer can reduce the magnitude of the seasonal variability of heat flux. Using MITgcm, W22 also found the seasonal cycle of the turbulent heat flux to have minimum magnitude in April and maximum in August; however, the annual mean value is larger by approximately a factor of two. They also reported the seasonal cycle of $z_{\max}$ with a minimum in April.

The reasonable agreement in the seasonal cycle of the heat flux between the new parameterization and the χ-pod values returns attention to the possible scaling of J_q with the product of u_*^2 and some form of local shear rate in the MI layer as suggested in previous studies. For example, M89 and Moum et al. (2023, hereafter M23) introduced a scaling of the dissipation

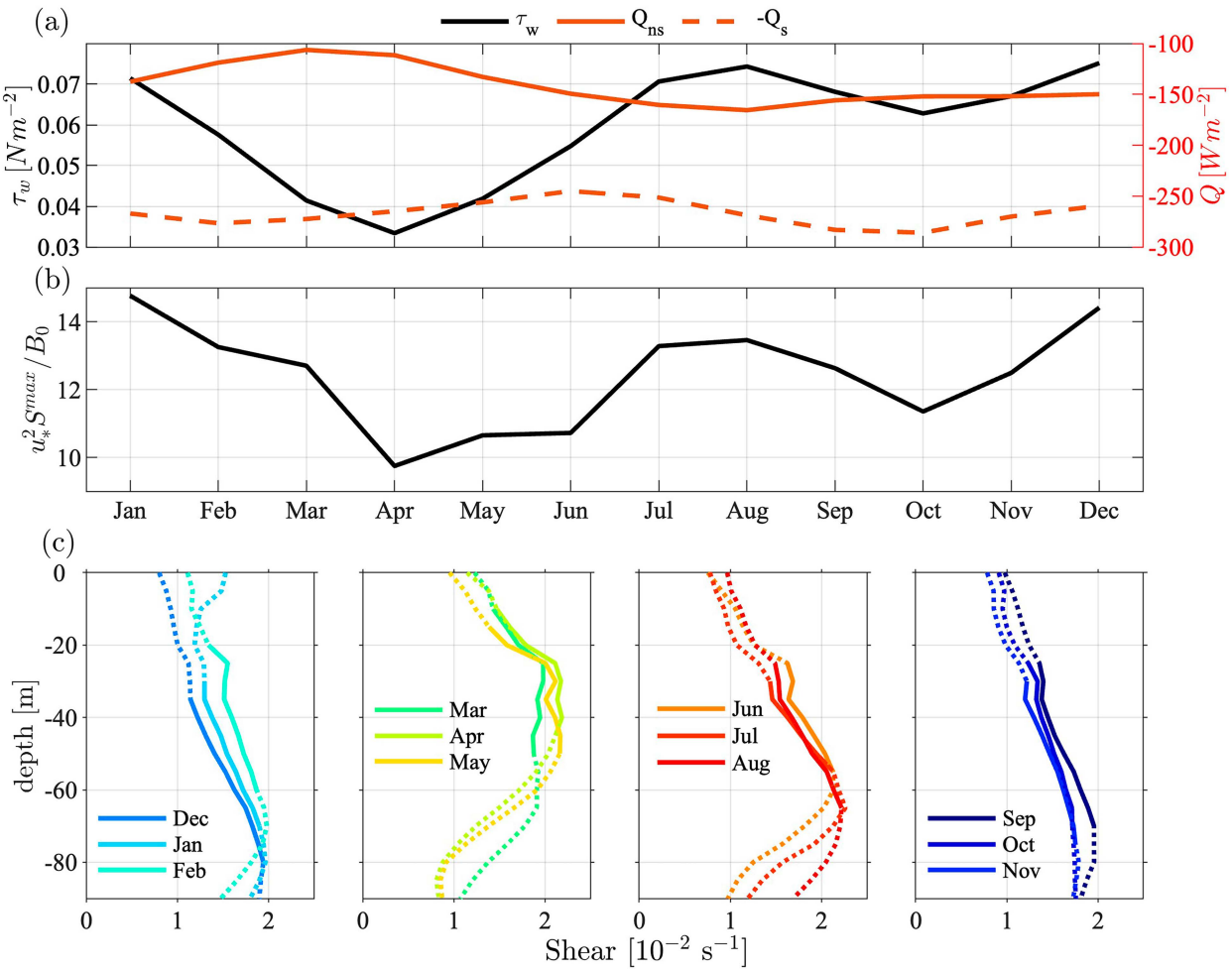

FIG. 13. Seasonal variability of (a) wind stress (τ_w) and solar (Q_s) and nonsolar (Q_{ns}) surface heat fluxes, (b) the ratio $u_*^2 S^{max}/B_0$, and (c) the shear profiles. The variability was obtained as monthly averages from a long observational record (May 1990–April 2020) at 0°, 140°W TAO mooring. Solid lines in (c) highlight the values inside the MI layer (i.e., from MLD to z^{MI}).

rate in the DCL that can also be used to parameterize the heat flux as follows:

$$\overline{J}_{q,p1} = -0.2\Gamma \frac{\rho_0 c_p}{\alpha g} u_*^2 S^b, \tag{12}$$

where S^b is the depth-averaged shear and the flux coefficient Γ is taken to be 0.2 (Osborn 1980). The appropriate parameterization of Γ is a subject of current debate. In a comprehensive review, Gregg et al. (2018) pointed out a wide range of values for Γ. The values of Γ observed at the TAO mooring vary between 0.12 and 0.48 (M89). The Γ values in our LES fall in the higher end of that range. Gregg et al. (2018) suggested $\Gamma = 0.2$, and Smyth (2020) explained why that value is to be expected in the MI turbulence regime. When comparing with previous studies, we therefore use $\Gamma = 0.2$ to infer turbulent heat fluxes from dissipation rates. The combination $\rho_0 c_p/\alpha g$ is fixed at 1.5×10^9 J s^2 m^{-4} (though it varies by up to ~10% over the depth range considered). The seasonal cycle of $\overline{J}_{q,p1}$ shown in Fig. 14b also indicates the weaker heat fluxes during spring and fall, and they get stronger during summer and winter. However, their amplitudes are considerably smaller than the $J_{q,p}$ values in the present study, possibly due to the use of depth-averaging S and ε.

We (i.e., S21) introduced the following scaling from analyzing the χ-pod data at the 0°, 140°W TAO mooring:

$$\overline{J}_{q,p2} = -0.0414\Gamma \frac{\rho_0 c_p}{\alpha g} \frac{(\mathbf{S}^b \cdot \boldsymbol{\tau}_w/\rho_0)^2}{|B_{sw}|}, \tag{13}$$

where B_{sw} is the surface short-wave buoyancy flux and the misalignment between the wind and the EUC shear is accounted for by the dot product. The result is set to zero if $\mathbf{S}^b \cdot \boldsymbol{\tau}_w$ is negative. In a comprehensive analysis of χ-pod data from both Pacific and Atlantic cold tongues, M23 suggested that the dot product in Eq. (13) is insufficient to represent the effects of wind shear misalignment. Pending a more detailed study, M23 substituted the simpler form:

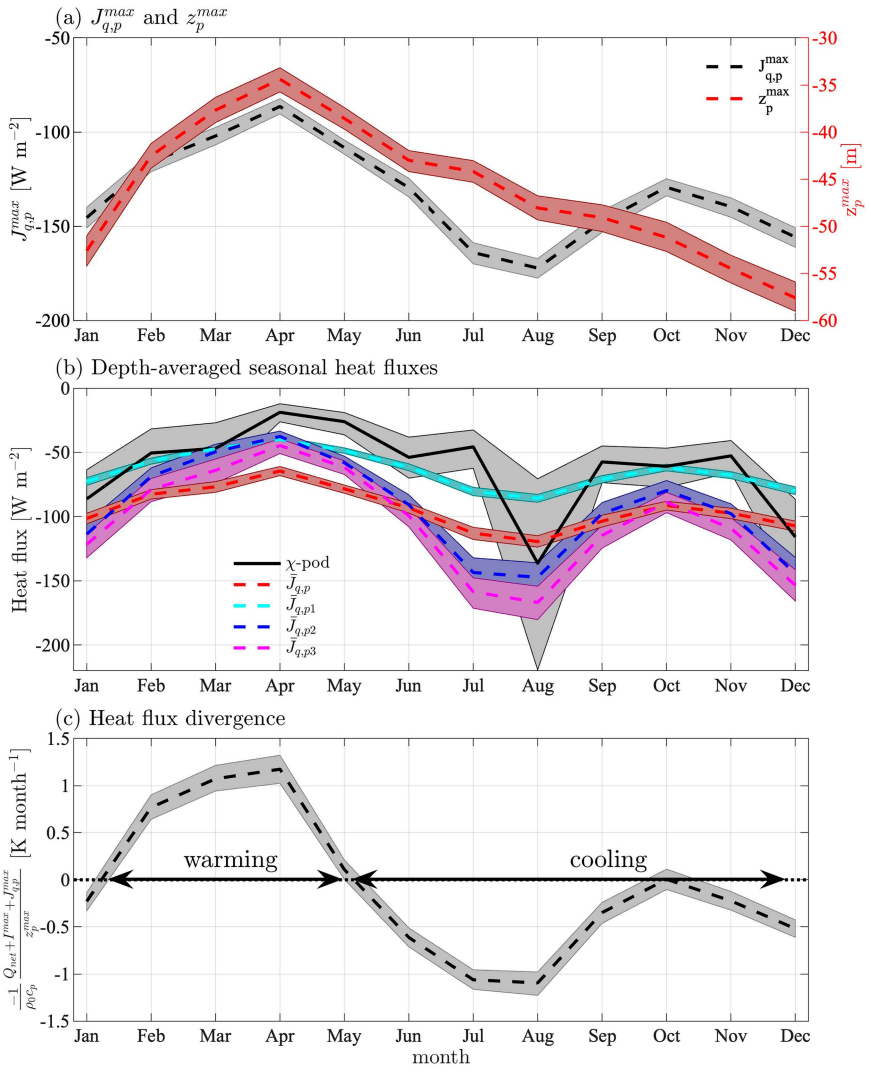

FIG. 14. Seasonality of parameterized heat fluxes: (a) peak heat flux ($J_{p,q}^{\max}$) and its depth ($z_p^{\max}$) and (b) depth-averaged values. (c) The heat flux divergence between the surface and $z^{\max}$. Panel (b) includes the heat fluxes from χ-pod measurements and previous parameterization studies [see Eqs. (12)–(14)]. Shading shows the 95% bootstrap confidence limits on the mean for each month.

$$\bar{J}_{q,p3} = -0.04\Gamma\frac{\rho_0 c_p}{\alpha g}\frac{(u_*^2 S^b)^2}{|B_{sw}|}. \tag{14}$$

By raising the product of wind and shear to the power 2, the parameterized heat fluxes $\bar{J}_{q,p2}$ and $\bar{J}_{q,p3}$ shown in Fig. 14b show improved agreement with the χ-pod measurement. Both Eqs. (13) and (14) are able to capture the observed local minima of heat flux intensity in spring and autumn and the local maxima in summer and winter. Their peak-to-peak (April–July) amplitudes also agree well with the measured values.

In our S21 study, the parameterization was based on dimensional analysis in which the correlation of the observed dissipation rate with $(u_*^2 S^b)^2$ proved stronger than that with $u_*^2 S^b$. Based on the analysis of TKE budget terms, we find the momentum flux $\langle u'w'\rangle$ and the dominant TKE budget terms (i.e., production, dissipation and buoyancy flux) at $z^{\max}$ scale well with u_*^2 and $u_*^2 S^{\max}$, respectively. Although the present parameterization does not agree with the χ-pod measurement as well as the S21 parameterization does quantitatively, it indeed captures the observed seasonal cycles of the heat flux. We note the time span of the χ-pod deployment (from 2005 to 2019) is different from the time span of the TAO mooring data (from 1990 to 2020) which are used to obtain the parameterized heat fluxes and also that there are numerous other uncertainties which make it difficult to objectively evaluate the performance of different parameterizations. Nonetheless, the present study adds to S21 and W22 by considering additive combinations of wind, shear and buoyancy effects and furthermore highlighting how the spatial distribution

of shear is important in the parameterization approach. Due to the coarse spatial resolution of the χ-pod deployment, the S21 parameterization required vertical averaging of the observed dissipation and shear before performing regression analysis. Vertical averaging tends to deteriorate correlation. When we attempt to correlate the depth-averaged dissipation with the depth-averaged shear using the LES data as we did in S21, we find the correlation coefficient is considerably weaker relative to correlating $\varepsilon^{\max}$ with $S^{\max}$ (not shown).

A unique feature of the new parameterization that S21 and M23 do not consider is the vertical distribution of the heat flux. Since the seasonal variability of the upper-ocean surface layer depends on the divergence of the heat flux, the vertical distribution of J_q helps improve the understanding of warming/cooling trend of the layer throughout the seasonal cycle. Within the context of vertical transport (i.e., neglecting lateral advection which can be significant), the temperature tendency can be approximated as follows:

$$\frac{\partial T_{\text{avg}}}{\partial t} = \frac{-1}{\rho_0 c_p} \frac{Q_{\text{net}} + I^{\max} + J_{q,p}^{\max}}{z_p^{\max}}, \tag{15}$$

where T_{avg} is the depth-averaged temperature, Q_{net} is the net daily surface heat flux into the ocean and $I^{\max}$ is the penetrative solar heat flux at $z^{\max}$ assuming Jerlov water type IB (Paulson and Simpson 1977; Simonot and Le Treut 1986). Note that the sign of $J_{q,p}^{\max}$ is negative, i.e., turbulence acts to transport heat downward from the EUC layer—a cooling influence. The heat flux difference $-(Q_{\text{net}} + I^{\max})$ is indicated by the markers at $z = 0$ in Fig. 12c.

We use daily profiles of $J_{q,p}$ and Eq. (15) to first obtain the temperature tendency *at daily time scale and then average in time* to deduce the tendency at seasonal time scale as shown in Fig. 14c. The present parameterization suggests the ocean surface layer is significantly warmed from February to April followed by a period of significant cooling between June and September. There is a net surface layer cooling trend across the annual cycle which agrees with the analysis in Moum et al. (2013).

There are similarities and differences between W22 and the present study, both of which use LES to develop parameterizations. W22 introduced a vertically varying parameterization for the daily averaged turbulent buoyancy flux that involves the peak buoyancy flux and the depth at which it occurs. The parameterization can be written in the context of heat flux as follows:

$$J_{q,\text{W22}}^{\max} = -0.16 \frac{\rho_0 c_p}{\alpha g} u_*^{2.05} (S^b)^{0.98}, \tag{16}$$

where S^b is the bulk shear defined by a least squares linear fit to the LES daily mean and horizontally averaged velocity profile from 5-m depth to the H_{Rig} depth where the gradient Richardson number exceeds 0.35. For the depth of the peak heat flux, W22 suggested the following scheme:

$$z_{\text{W22}}^{\max} = 0.6 H_{\text{Rib}} - 14, \tag{17}$$

where H_{Rib} is the depth where the bulk Richardson number (Ri_b) exceeds 0.2. The H_{Rib} depth was obtained by using the formulation introduced in the KPP turbulent mixing parameterization (Large et al. 1994; Smyth et al. 2002). It should be noted that $z_{\text{W22}}^{\max}$ and H_{Rib} take negative values to be consistent with the notation used in the present study (W22 defined $z_{\text{W22}}^{\max}$ and H_{Rib} with positive values). Comparing Eq. (7) to Eq. (16), the present parameterization and that of W22 take the same functional form but three differences are noted: 1) the proportionality constant is larger in Eq. (16), 2) the dependence on B_0 is omitted, and 3) a bulk shear (S^b instead of $S^{\max}$) is used by W22. Furthermore, comparing Eq. (11) to Eq. (17), the W22 parameterization relies on the velocity and temperature profiles in the surface mixed layer to locate $z^{\max}$ while the present study uses the flow condition that is local to the MI layer to identify that depth. Due to the lack of observations in the near-surface layer, we are unable to include the heat flux from the W22 parameterization in Fig. 14. Last, we note that the W22 parameterization was obtained using the LES simulations of DCT both on and off the equator while our simulations focus on the former.

6. Discussion and conclusions

We have performed a parametric study using LES to identify the processes that influence the DCT in the equatorial Pacific at multiple time scales. DCT is known to occur mostly at nighttime in the marginal instability (MI) layer above the Equatorial Undercurrent (EUC) core. Measurements from the χ-pods deployed at 0°, 140°W between 2005 and 2011 reveal a seasonal cycle of subsurface heat flux driven by DCT that can warm the surface mixed layer (ML) during spring while cooling it during autumn (Moum et al. 2013). We are interested in finding the key physical parameters that affect the heat flux at daily and seasonal time scales. In the LES, we systematically vary surface convective cooling flux (Q_{ns}), wind stress (τ_w), initial thickness (h_{MI}) and shear magnitude (S) of the MI layer over a wide range of observed values. Each case is simulated for a period of 24 h to characterize DCT with high resolution at multiple time scales and to also obtain the daily averaged heat flux (J_q) profile. The daily averaged J_q profiles from the 27 LES cases are analyzed to deduce a new heat flux parameterization that is then demonstrated to provide a reasonable prediction of the seasonal cycle of J_q.

Nighttime DCT exhibits significant variability with multiple bursts of turbulence that persist into the following morning. Among the four control parameters, τ_w and S are found to most strongly influence daily averaged values of J_q. Increasing τ_w and S generally increases J_q. Increasing h_{MI} also tends to increase J_q albeit not as strongly as τ_w and S. Increasing convection slightly enhances the heat flux.

Using the LES results, we formulate a new parameterization for daily averaged turbulent heat flux ($J_{q,p}$) that accounts for the effects of the four forcing parameters. This parameterization is summarized in section 4c. Unlike our previous parameterization in S21 and, improving upon that proposed in W22, it uses the local shear within the MI layer along with τ_w and surface cooling flux to infer the heat fluxes at MLD as well as at the depth $z^{\max}$ where J_q is largest. Heat fluxes at both depths are assumed to be bilinearly proportional to

$u_*^2 S^{\max}$ and B_0, where u_* is frictional velocity, $S^{\max}$ is the local shear rate, and B_0 is the surface convective buoyancy flux [see Eqs. (7), (9), and (11)]. Effects of the thickness of the MI layer are implicitly included in the parameterization through the locations of MLD and the bottom of the MI layer (z^{MI}) where $\mathrm{Ri}_g > 0.3$. A piecewise linear profile, based on the heat fluxes at MLD (location known from data), at $z^{\max}$ (location known through proposed parameterization) and the value of zero heat flux at z^{MI} (location known through data and the criterion of $\mathrm{Ri}_g = 0.3$), provides a model $J_{q,p}(z)$. Integration of $J_{q,p}(z)$ over the MI depth range leads to a bulk value of J_q which is then compared to observational data and previous parameterizations.

The present LES-based parameterization builds upon previous studies (i.e., M89; S21; W22; M23) by parameterizing the vertical distribution of the turbulent heat flux and its annual variation in terms of a bilinear combination of buoyancy flux and the product of wind stress and current shear. We apply the new parameterization using TAO mooring data, and the result shows reasonable agreement with χ-pod measurements (see Fig. 14). The peak heat flux values, and the depths at which they occur suggest that strong seasonal cooling during the summer months (June–August) leads to a net annual cooling similar to the observed trend previously reported by Moum et al. (2013). Although the new parameterization includes the effects of convection, its contribution to the seasonal cycle of heat fluxes is usually secondary. The contribution of convection can be larger during periods with weak winds such as the onset of El Niño events (Luther et al. 1983).

Different from M89, S21, and M23, whose parameterizations target the depth-averaged dissipation rate, the new parameterization describes the vertical distribution of the turbulent heat flux as does W22. Although both W22 and the new parameterization propose scaling by the friction velocity and local shear, the new parameterization is calibrated using shear local to the MI layer while the sheared region in W22 extends to include the mixed layer. The parameterization of $z^{\max}$ is also calibrated here using the available flow quantities inside the MI layer, while the $z^{\max}$ in W22 requires information in the surface mixed layer. Since the data at the TAO mooring is limited in the surface mixed layer, the new parameterization improves upon the W22 scheme by circumventing those limitations.

As with any proposed parameterization, it is important to point out its uncertainties. Unlike the LES in W22 and Wang et al. (1998), which includes the effects of large-scale forcing terms, the LES in the present study does not account for the turbulent mixing in the MI layer that can be driven by other processes such as lateral advection. The use of uniform shear and uniform stratification in the initial condition and constant surface fluxes throughout the simulation is an explicit choice made to better understand their physical effect on DCT turbulence and also to reduce the number of control parameters in the scaling analysis. Note that the range of shear, stratification, and surface forcing is sufficient to represent a seasonal cycle in observations. Spatial variability of shear and stratification and temporal variability in the surface forcing can affect the regression coefficients. The new parameterization allows exploration of the spatial and temporal variability of turbulent heat fluxes at the daily time scale and longer. The parameterization is not designed for shorter-than-daily time scales, e.g., it is not a mixing model for prognostic calculations at the time stepping scales used in GCMs.

We have not explored the effect of solar heat fluxes and other turbulent processes in the ML such as Langmuir circulations, breaking waves, and tides, etc. In the limit of low wind speed ($U_{10} \leq 2\ \mathrm{m\ s^{-1}}$), a diurnal warm layer (DWL) can form and alter the evolution of turbulence in the ML during daytime (e.g., Hughes et al. 2020a). When the DWL dissipates in the afternoon, the resulting turbulence can affect the descending shear layer and, thus, the instantaneous intensity of the DCT. Breaking surface waves and Langmuir circulations can also enhance ML turbulence (Sullivan et al. 2007; Grant and Belcher 2009; Li and Fox-Kemper 2017) and, by changing the divergence of turbulent momentum transport between the ML and the DCL, modify DCT. Internal waves in the DCL can be excited by Langmuir circulations (Polton et al. 2008) and shear instabilities (Pham et al. 2009; Pham and Sarkar 2010). It remains unknown how these internal waves or internal waves propagating into the sheared zone from deeper water would influence the DCT. Whether these additional phenomena would affect the quality of the present parameterization over the seasonal time scale requires future study.

Acknowledgments. We are grateful for the support provided by National Foundation Science Grants OCE-1851390 for HTP and SS, and OCE-1851520 for WDS, JNM and SW. JNM also acknowledges the support by National Foundation Science Grants OCE-2048631 and 2049145. Computing support on Gaffney and Koehr was provided by High Performance Computing Modernization Program sponsored by the U.S. Department of Defense.

Data availability statement. Data are published and a link is provided in Pham (2024). Software necessary to reproduce the figures will be published upon acceptance.

REFERENCES

Cherian, D. A., D. B. Whitt, R. M. Holmes, R.-C. Lien, S. D. Bachman, and W. G. Large, 2021: Off-equatorial deep-cycle turbulence forced by tropical instability waves in the equatorial Pacific. *J. Phys. Oceanogr.*, **51**, 1575–1593, https://doi.org/10.1175/JPO-D-20-0229.1.

Ducros, F., P. Comte, and M. Lesieur, 1996: Large-eddy simulation of transition to turbulence in a boundary layer developing spatially over a flat plate. *J. Fluid Mech.*, **326**, 1–36, https://doi.org/10.1017/S0022112096008221.

Grant, A. L. M., and S. E. Belcher, 2009: Characteristics of Langmuir turbulence in the ocean mixed layer. *J. Phys. Oceanogr.*, **39**, 1871–1887, https://doi.org/10.1175/2009JPO4119.1.

Gregg, M. C., E. A. D'Asaro, J. J. Riley, and E. Kunze, 2018: Mixing efficiency in the ocean. *Annu. Rev. Mar. Sci.*, **10**, 443–473, https://doi.org/10.1146/annurev-marine-121916-063643.

Hebert, D., J. N. Moum, C. A. Paulson, and D. R. Caldwell, 1992: Turbulence and internal waves at the equator. Part II: Details of a single event. *J. Phys. Oceanogr.*, **22**, 1346–1356, https://

doi.org/10.1175/1520-0485(1992)022%3C1346:TAIWAT%3E2.0.CO;2.

Hughes, K. G., J. N. Moum, and E. L. Shroyer, 2020a: Evolution of the velocity structure in the diurnal warm layer. *J. Phys. Oceanogr.*, **50**, 615–631, https://doi.org/10.1175/JPO-D-19-0207.1.

——, ——, and ——, 2020b: Heat transport through diurnal warm layers. *J. Phys. Oceanogr.*, **50**, 2885–2905, https://doi.org/10.1175/JPO-D-20-0079.1.

——, ——, ——, and W. D. Smyth, 2021: Stratified shear instabilities in diurnal warm layers. *J. Phys. Oceanogr.*, **51**, 2583–2598, https://doi.org/10.1175/JPO-D-20-0300.1.

Jacobitz, F. G., S. Sarkar, and C. W. VanAtta, 1997: Direct numerical simulations of the turbulence evolution in a uniformly sheared and stably stratified flow. *J. Fluid Mech.*, **342**, 231–261, https://doi.org/10.1017/S0022112097005478.

Large, W. G., and P. R. Gent, 1999: Validation of vertical mixing in an equatorial ocean model using large eddy simulations and observations. *J. Phys. Oceanogr.*, **29**, 449–464, https://doi.org/10.1175/1520-0485(1999)029%3C0449:VOVMIA%3E2.0.CO;2.

——, J. C. McWilliams, and S. C. Doney, 1994: Oceanic vertical mixing: A review and a model with a nonlocal boundary layer parameterization. *Rev. Geophys.*, **32**, 363–403, https://doi.org/10.1029/94RG01872.

Lefauve, A., J. L. Partridge, and P. F. Linden, 2019: Regime transitions and energetics of sustained stratified shear flows. *J. Fluid Mech.*, **875**, 657–698, https://doi.org/10.1017/jfm.2019.488.

Li, Q., and B. Fox-Kemper, 2017: Assessing the effects of Langmuir turbulence on the entrainment buoyancy flux in the ocean surface boundary layer. *J. Phys. Oceanogr.*, **47**, 2863–2886, https://doi.org/10.1175/JPO-D-17-0085.1.

Lien, R.-C., D. R. Caldwell, M. C. Gregg, and J. N. Moum, 1995: Turbulence variability at the equator in the central Pacific at the beginning of the 1991–1993 El Niño. *J. Geophys. Res.*, **100**, 6881–6898, https://doi.org/10.1029/94JC03312.

——, M. J. McPhaden, and M. C. Gregg, 1996: High-frequency internal waves at 0°, 140°W and their possible relationship to deep-cycle turbulence. *J. Phys. Oceanogr.*, **26**, 581–600, https://doi.org/10.1175/1520-0485(1996)026%3C0581:HFIWAA%3E2.0.CO;2.

Liu, C.-L., A. K. Kaminski, and W. D. Smyth, 2022: The butterfly effect and the transition to turbulence in a stratified shear layer. *J. Fluid Mech.*, **953**, A43, https://doi.org/10.1017/jfm.2022.985.

Lombardo, C. P., and M. C. Gregg, 1989: Similarity scaling of viscous and thermal dissipation in a convecting surface boundary layer. *J. Geophys. Res.*, **94**, 6273–6284, https://doi.org/10.1029/JC094iC05p06273.

Luther, D. S., D. E. Harrison, and R. A. Knox, 1983: Zonal winds in the central equatorial Pacific and El Niño. *Science*, **222**, 327–330, https://doi.org/10.1126/science.222.4621.327.

Moulin, A. J., J. N. Moum, E. L. Shroyer, and M. Hoecker-Martínez, 2021: Freshwater lens fronts propagating as buoyant gravity currents in the equatorial Indian Ocean. *J. Geophys. Res. Oceans*, **126**, e2021JC017186, https://doi.org/10.1029/2021JC017186.

Moum, J. N., and D. R. Caldwell, 1985: Local influences on shear-flow turbulence in the equatorial ocean. *Science*, **230**, 315–316, https://doi.org/10.1126/science.230.4723.315.

——, ——, and C. A. Paulson, 1989: Mixing in the equatorial surface layer and thermocline. *J. Geophys. Res.*, **94**, 2005–2022, https://doi.org/10.1029/JC094iC02p02005.

——, A. Perlin, J. D. Nash, and M. J. McPhaden, 2013: Seasonal sea surface cooling in the equatorial Pacific cold tongue controlled by ocean mixing. *Nature*, **500**, 64–67, https://doi.org/10.1038/nature12363.

——, and Coauthors, 2022: Deep cycle turbulence in Atlantic and Pacific cold tongues. *Geophys. Res. Lett.*, **49**, e2021GL097345, https://doi.org/10.1029/2021GL097345.

——, W. D. Smyth, K. G. Hughes, D. Cherian, S. J. Warner, B. Bourlès, P. Brandt, and M. Dengler, 2023: Wind dependencies of deep cycle turbulence in the equatorial cold tongues. *J. Phys. Oceanogr.*, **53**, 1979–1995, https://doi.org/10.1175/JPO-D-22-0203.1.

Osborn, T. R., 1980: Estimates of the local rate of vertical diffusion from dissipation measurements. *J. Phys. Oceanogr.*, **10**, 83–89, https://doi.org/10.1175/1520-0485(1980)010%3C0083:EOTLRO%3E2.0.CO;2.

Paulson, C. A., and J. J. Simpson, 1977: Irradiance measurements in the upper ocean. *J. Phys. Oceanogr.*, **7**, 952–956, https://doi.org/10.1175/1520-0485(1977)007%3C0952:IMITUO%3E2.0.CO;2.

Pearson, B. C., A. L. M. Grant, J. A. Polton, and S. E. Belcher, 2015: Langmuir turbulence and surface heating in the ocean surface boundary layer. *J. Phys. Oceanogr.*, **45**, 2897–2911, https://doi.org/10.1175/JPO-D-15-0018.1.

Pei, S., T. Shinoda, W. Wang, and R.-C. Lien, 2020: Simulation of deep cycle turbulence by a global ocean general circulation model. *Geophys. Res. Lett.*, **47**, e2020GL088384, https://doi.org/10.1029/2020GL088384.

Perlin, A., and J. N. Moum, 2012: Comparison of thermal variance dissipation rates from moored and profiling instruments at the equator. *J. Atmos. Oceanic Technol.*, **29**, 1347–1362, https://doi.org/10.1175/JTECH-D-12-00019.1.

Pham, H. T., 2024: Data and software for "Deep-cycle turbulence in the upper Pacific Equatorial Ocean: characterization by LES and heat flux parameterization." Zenodo, https://doi.org/10.5281/zenodo.10552971.

——, and S. Sarkar, 2010: Internal waves and turbulence in a stable stratified jet. *J. Fluid Mech.*, **648**, 297–324, https://doi.org/10.1017/S0022112009993120.

——, ——, and K. A. Brucker, 2009: Dynamics of a stratified shear layer above a region of uniform stratification. *J. Fluid Mech.*, **630**, 191–223, https://doi.org/10.1017/S0022112009006478.

——, ——, and K. B. Winters, 2013: Large-eddy simulation of deep-cycle turbulence in an equatorial undercurrent model. *J. Phys. Oceanogr.*, **43**, 2490–2502, https://doi.org/10.1175/JPO-D-13-016.1.

——, W. D. Smyth, S. Sarkar, and J. N. Moum, 2017: Seasonality of deep-cycle turbulence in the eastern equatorial Pacific. *J. Phys. Oceanogr.*, **47**, 2189–2209, https://doi.org/10.1175/JPO-D-17-0008.1.

——, S. Sarkar, L. Johnson, B. Fox-Kemper, P. P. Sullivan, and Q. Li, 2023: Multi-scale temporal variability of turbulent mixing during a monsoon intra-seasonal oscillation in the Bay of Bengal: An LES study. *J. Geophys. Res. Oceans*, **128**, e2022JC018959, https://doi.org/10.1029/2022JC018959.

Polton, J. A., J. A. Smith, J. A. MacKinnon, and A. E. Tejada-Martínez, 2008: Rapid generation of high-frequency internal waves beneath a wind and wave forced oceanic surface mixed layer. *Geophys. Res. Lett.*, **35**, L13602, https://doi.org/10.1029/2008GL033856.

Price, J. F., R. A. Weller, and R. Pinkel, 1986: Diurnal cycling: Observations and models of the upper ocean response to

diurnal heating, cooling, and wind mixing. *J. Geophys. Res.*, **91**, 8411–8427, https://doi.org/10.1029/JC091iC07p08411.

Sarkar, S., and H. T. Pham, 2019: Turbulence and thermal structure in the upper ocean: Turbulence-resolving simulations. *Flow Turbul. Combust.*, **103**, 985–1009, https://doi.org/10.1007/s10494-019-00065-5.

Simonot, J.-Y., and H. Le Treut, 1986: A climatological field of mean optical properties of the world ocean. *J. Geophys. Res.*, **91**, 6642–6646, https://doi.org/10.1029/JC091iC05p06642.

Skyllingstad, E. D., W. D. Smyth, J. N. Moum, and H. Wijesekera, 1999: Upper-ocean turbulence during a westerly wind burst: A comparison of large-eddy simulation results and microstructure measurements. *J. Phys. Oceanogr.*, **29**, 5–28, https://doi.org/10.1175/1520-0485(1999)029%3C0005:UOTDAW%3E2.0.CO;2.

Smith, K. M., C. P. Caulfield, and J. R. Taylor, 2021: Turbulence in forced stratified shear. *J. Fluid Mech.*, **910**, A42, https://doi.org/10.1017/jfm.2020.994.

Smyth, W. D., 2020: Marginal instability and the efficiency of ocean mixing. *J. Phys. Oceanogr.*, **50**, 2141–2150, https://doi.org/10.1175/JPO-D-20-0083.1.

——, and J. N. Moum, 2013: Marginal instability and deep cycle turbulence in the eastern equatorial Pacific Ocean. *Geophys. Res. Lett.*, **40**, 6181–6185, https://doi.org/10.1002/2013GL058403.

——, P. O. Zavialov, and J. N. Moum, 1997: Decay of turbulence in the upper ocean following sudden isolation from surface forcing. *J. Phys. Oceanogr.*, **27**, 810–822, https://doi.org/10.1175/1520-0485(1997)027%3C0810:DOTITU%3E2.0.CO;2.

——, J. N. Moum, and D. R. Caldwell, 2001: The efficiency of mixing in turbulent patches: Inferences from direct simulations and microstructure observations. *J. Phys. Oceanogr.*, **31**, 1969–1992, https://doi.org/10.1175/1520-0485(2001)031%3C1969:TEOMIT%3E2.0.CO;2.

——, E. D. Skyllingstad, G. B. Crawford, and H. Wijesekera, 2002: Nonlocal fluxes and Stokes drift effects in the K-profile parameterization. *Ocean Dyn.*, **52**, 104–115, https://doi.org/10.1007/s10236-002-0012-9.

——, J. N. Moum, and J. D. Nash, 2011: Narrowband oscillations in the upper equatorial ocean. Part II: Properties of shear instabilities. *J. Phys. Oceanogr.*, **41**, 412–428, https://doi.org/10.1175/2010JPO4451.1.

——, ——, L. Li, and S. A. Thorpe, 2013: Diurnal shear instability, the descent of the surface shear layer, and the deep cycle of equatorial turbulence. *J. Phys. Oceanogr.*, **43**, 2432–2455, https://doi.org/10.1175/JPO-D-13-089.1.

——, H. T. Pham, J. N. Moum, and S. Sarkar, 2017: Pulsating turbulence in a marginally unstable stratified shear flow. *J. Fluid Mech.*, **822**, 327–341, https://doi.org/10.1017/jfm.2017.283.

——, S. J. Warner, J. N. Moum, H. T. Pham, and S. Sarkar, 2021: What controls the deep cycle? Proxies for equatorial turbulence. *J. Phys. Oceanogr.*, **51**, 2291–2302, https://doi.org/10.1175/JPO-D-20-0236.1.

Sullivan, P. P., J. C. McWilliams, and W. K. Melville, 2007: Surface gravity wave effects in the oceanic boundary layer: Large-eddy simulation with vortex force and stochastic breakers. *J. Fluid Mech.*, **593**, 405–452, https://doi.org/10.1017/S002211200700897X.

Thompson, E. J., J. N. Moum, C. W. Fairall, and S. A. Rutledge, 2019: Wind limits on rain layers and diurnal warm layers. *J. Geophys. Res. Oceans*, **124**, 897–924, https://doi.org/10.1029/2018JC014130.

VanDine, A., H. T. Pham, and S. Sarkar, 2021: Turbulent shear layers in a uniformly stratified background: DNS at high Reynolds number. *J. Fluid Mech.*, **916**, A42, https://doi.org/10.1017/jfm.2021.212.

Wang, D., and P. Müller, 2002: Effects of equatorial undercurrent shear on upper-ocean mixing and internal waves. *J. Phys. Oceanogr.*, **32**, 1041–1057, https://doi.org/10.1175/1520-0485(2002)032%3C1041:EOEUSO%3E2.0.CO;2.

——, J. C. McWiliams, and W. G. Large, 1998: Large-eddy simulation of the diurnal cycle of deep equatorial turbulence. *J. Phys. Oceanogr.*, **28**, 129–148, https://doi.org/10.1175/1520-0485(1998)028%3C0129:LESOTD%3E2.0.CO;2.

Warner, S. J., and J. N. Moum, 2019: Feedback of mixing to ENSO phase change. *Geophys. Res. Lett.*, **46**, 13 920–13 927, https://doi.org/10.1029/2019GL085415.

Wenegrat, J. O., and M. J. McPhaden, 2015: Dynamics of the surface layer diurnal cycle in the equatorial Atlantic Ocean (0°, 23°W). *J. Geophys. Res. Oceans*, **120**, 563–581, https://doi.org/10.1002/2014JC010504.

Whitt, D. B., 2022: Rain impacts on the surface atmosphere and upper ocean in the central equatorial Pacific. *J. Phys. Oceanogr.*, **52**, 1969–1991, https://doi.org/10.1175/JPO-D-22-0033.1.

——, D. A. Cherian, R. M. Holmes, S. D. Bachman, R.-C. Lien, W. G. Large, and J. N. Moum, 2022: Simulation and scaling of the turbulent vertical heat transport and deep-cycle turbulence across the equatorial Pacific cold tongue. *J. Phys. Oceanogr.*, **52**, 981–1014, https://doi.org/10.1175/JPO-D-21-0153.1.